

Statistical Emulation of Human Operational Motions

Yanliang Chen

Dept of Statistics, Florida State University, Tallahassee, FL 32306 ychen23@fsu.edu

Chiwoo Park

Dept of Industrial and Systems Engineering, University of Washington, Seattle, WA 98195, chiwpark@uw.edu

Anuj Srivastava

Dept of Statistics, Florida State University, Tallahassee, FL 32306 anuj@stat.fsu.edu

Abstract. This paper addresses the critical and challenging task of developing emulators for simulating human operational motions in industrial workplaces. We conceptualize human motion as a sequence of human body shapes. Leveraging statistical shape theory, we develop statistical generative models for sequences of human (body) shapes of human workers in workplaces. Our goal is to create emulators that generate random, realistic human motions statistically consistent with past work performances, essential for simulating industrial operations involving human labor. We derive the space of shapes as a Riemannian shape manifold, modeling human motion as a continuous-time stochastic process on this manifold. Representing such processes is challenging due to the nonlinearity of the shape manifold, variability in execution rates across observations, infinite dimensionality of stochastic processes, and population variability within and across action classes. This paper studies multiple solutions to these problems. This paper proposes multiple solutions to these challenges, presenting a comprehensive framework that incorporates (1) time warping for temporal alignment of training data, (2) Riemannian geometry for tackling manifold nonlinearity, and (3) Shape- and Functional-PCA for dimension reduction leading to traditional finite-dimensional Euclidean representations. In particular, it develops the transported velocity field representation for motion sequences and imposes a Gaussian model on the resulting Euclidean spaces. It then applies these models to emulate human shape sequences from an industrial operation dataset and evaluates these simulations in multiple ways.

Key words: motion and time study, statistical shape analysis, sequence of shapes, human activity models

1. Introduction

This paper presents new statistical models and algorithms to emulate human operational motions using models trained from past observations. The new methods will model the statistical variations inherent in actual human motion data, providing an understanding of statistical variations in past human operational motions, which form the basis of the *motion-and-time studies* in operations research (Barnes 1949).

Moreover, the statistical emulator will enable a model-based simulation of human operations. This simulator is crucial for creating digital twins of industrial operations in settings like factories, hospitals, and other workplaces that heavily depend on human workers. Although robots and machines automate many tasks, typical workplaces still involve a complex mix of automated and manual operations, relying heavily

on human operators. Human operations often introduce significant process variations due to worker errors, fatigue, and insufficient training (Hendrich et al. 2008, Urgo et al. 2019). The operational uncertainties in manual operations are seldom quantified and integrated into digital twin models for operations planning and optimization (Park et al. 2022). The proposed digital emulator would provide a statistical tool to incorporate human-related process variations into a digital twin of systems involving human work. In this paper, we utilize motion data from five classes of manufacturing operations from an industrial dataset (Park et al. 2022) to study the motion emulator. Fig. 1c shows an example sub-sequence from this dataset.

There are two broad approaches to simulating human motions. One uses physical or biomechanical models that, in turn, rely on detailed dynamical systems with explicit constraints and physical laws built-in and apply input forces to predict or generate human motion (Xiang et al. 2010, 2012, da Silva et al. 2008, Park et al. 2019). These physical approaches rely on our prior understanding of physical interactions, often in the form of constrained differential equations. While these solutions are realistic, the approaches are specific to applications. They are not easily generalizable. The second approach is the data-driven approach, which utilizes and analyzes past observations of human operator’s motions. Several studies, including Zhang et al. (2014), Suhermi et al. (2018), Wang et al. (2018), Suhermi et al. (2018), Xu et al. (2019), have taken this approach to solve specific problems such as segmenting actions, modeling locomotion, or classifying actions. However, simulating long realistic sequences of complex human postures, including several segments performing diverse simple tasks, remains a distant goal. In this paper, a long sequence implies that an observation is a concatenation of several smaller actions performed by an agent. The overall activity represented by the full sequence is a composition of several smaller, simpler activities. The past works have mainly restricted to smaller sequences representing these individual small actions.

In this paper, we develop a data-driven approach to learning, modeling, and emulating long sequences of human operational movements. Toward that goal, we first develop proper data-driven representations of human postures and movements. Specifically, we utilize a shape representation of human posture (Park et al. 2022). As shown in Fig. 1a, the device records several landmark locations on the human body. We then extract shape features of these landmarks by discarding information unrelated to posture, such as global coordinate systems and body sizes. This requires formal mathematical representations of the landmark-based shapes of human postures. We define a shape space \mathcal{Y} (Park et al. 2022), whose elements represent the shapes of the human body; details will be described in Sec. 3.1. This shape space is a curved, non-Euclidean space, specifically a Riemannian manifold with a well-known intrinsic Riemannian metric. We view human motion as a time-indexed trajectory in this shape space. While the literature has extensively studied the shape analysis of static shapes or short sequences of shapes using Kendall’s shape analysis (Kendall 1989), analyzing and modeling long shape sequences presents significant challenges.

We will explore multiple modeling choices to overcome technical challenges in representing long shape sequences in the shape space \mathcal{Y} . Viewing a human motion sequence as a random realization of a stochastic

process X with instantaneous values in \mathcal{Y} , one can take a discrete-time approach by developing a time-series model (such as vector auto-regression (VAR)) or a continuous-time approach such as stochastic differential equation. Then, we need to impose a statistical model on the chosen space in a way that captures the observed patterns and is estimatable efficiently from data. One can choose a parametric approach, *e.g.*, a Gaussian process model, or a non-parametric approach, where each sample path is treated as an unstructured function. When it comes to modeling a sequence in the curved space \mathcal{Y} , there are two broad approaches: (1) modeling a shape sequence directly on \mathcal{Y} using its intrinsic Riemannian geometry, and (2) approximately flattening \mathcal{Y} into a Euclidean space (often a tangent space of \mathcal{Y}) that allows the use of traditional (Euclidean) statistical models. Since flattening introduces distortions in the underlying topology, ideally, one would model shapes intrinsically on \mathcal{Y} itself. However, the nonlinearity of \mathcal{Y} poses major challenges in modeling complex spatio-temporal patterns present in industrial activities. For instance, it becomes difficult to capture correlations between shapes across time. We explore various flattening ideas in Sec. 2.

In addition to the shape (spatial) variability in human postures, the sequences contain temporal variability caused by the different work speeds of different operators. It is essential to account for this variability when modeling with human motions. For example, it is known that aligning motion sequences significantly improves modeling and classification (Veeraraghavan et al. 2009, Amor et al. 2015). One way to remove temporal variability from the motion sequences is to use a reference motion and temporally align every motion sequence to the reference. We explore various alignment ideas in Sec. 2.

Lastly, different combinations of these choices lead to different solutions and performances. Therefore, we need to evaluate these modeling choices and select the best model for our application. We will assess these models in several ways: using visualizations, statistical likelihoods, non-parametric hypothesis tests, and specialized ideas. We apply these diverse ideas to a manufacturing dataset and present our findings. We also provide the strengths and limitations of different choices studied in these experiments.

The remainder of this paper is organized as follows. Sec. 2 reviews existing research directly related to the challenges discussed above, and Sec. 3 provides a background on the posture space and temporal alignment of the posture sequences. In Sec. 4, we explore different approaches to representing the pre-aligned motion sequences by flattening or working on the shape manifold. We perform dimension reduction to obtain a set of PCA coefficients for modeling under the flattening approach. We fit different statistical models to emulate new motion sequences for several representations. In addition, we introduce several evaluation metrics to compare the performance of the simulation. Sec. 5 shows the experiment results on different combinations of representations and modeling methods. Due to the limited data, we conduct experiments on sub-sequences and a two-level simulation to simplify the model. Finally, Sec. 6 summarizes our results and discusses future directions.

2. Literature Review

This section reviews current literature involving tools and techniques pertinent to our approach. While most existing research focuses on short-term activities or single actions (Zhang et al. 2014, Wang et al. 2018), we focus on methods that handle long sequences. Since the shapes of human postures naturally reside on a nonlinear manifold \mathcal{Y} , another focus is on statistical modeling and analysis of shape sequences.

Shape-Sequence Representation Space: As described in Sec. 3, the shape space \mathcal{Y} of human postures is a curved, Riemannian manifold endowed with a Riemannian structure that helps define geodesics, geodesic distances, means, and covariances for individual shapes. A common intrinsic approach to modeling stochastic processes on \mathcal{Y} is to model each time point independently (Sidenbladh et al. 2002). This simple approach neglects temporal correlation among human postures. The other common approach is to flatten the (curved) shape space \mathcal{Y} to a Euclidean space and then apply traditional vector-space modeling. A naïve flattening is through a *single inverse exponential map* (SIEM) that brings each shape $\mathbf{Y} \in \mathcal{Y}$ to a pre-determined reference shape (Yi et al. 2012). An alternative involves forming a velocity vector field, *i.e.*, the time derivatives of shape sequences. To reconcile velocity vectors at different locations, Su et al. (2014) parallel transported them to a reference point in a single-hop and called them *transported square-root velocity field* (TSRVF). These single-hop transports can lead to significant distortions in data when the data are spread far from the reference tangent space. Zhang et al. (2015) addressed the issue by utilizing multi-hop parallel transport. We refer to a single-hop parallel transport as *single-hop transported square-root velocity field* (S-TSRVF), and the multi-hops one as *multi-hop TSRVF* (M-TSRVF). Deng et al. (2021) worked with pre-aligned sequences and used a multi-hop *transported velocity field* (M-TVF). Due to repeated parallel transports, a multi-hop approach is prone to numerical errors that can become substantial for long sequences. Also, since TVF relates to the first derivative of a shape sequence, the observation noise gets amplified. We address this issue by taking the integral of TVF, called IS-TVF. This representation is closely related to *unrolling* and *unwrapping* ideas used by Jupp and Kent (1987) and Le (2003).

Temporal Alignments of Sequences: Shape sequences vary depending on the rates of action depicted in the sequences. For example, operators working at different speeds in human operational analysis introduce a lack of synchronization in the sequences. To synchronize sequence and focus on shape variability, we align them in pre-processing. Several methods have been proposed for this temporal alignment. Raptis and Sigal (2013) use landmarks for alignment and Veeraraghavan et al. (2009) used dynamic time warping (DTW). Su et al. (2014) used the TSRVF framework, which exploits the invariance properties of the \mathbb{L}^2 metric on the TSRVFs to time warping. Some other papers also use TSRVF for temporal alignment (Amor et al. 2015, Deng et al. 2021, Park et al. 2022). Celledoni et al. (2016) extended the approach to certain nonlinear manifolds and Le Brigant (2019) used a Sobolev metric instead of the standard \mathbb{L}^2 metric. This paper follows the TSRVF framework for pre-processing the temporal alignment.

Spatio-Temporal Dimension Reduction: Shape spaces, or even their flattened versions, are still high-dimensional, and one needs a dimension-reduction step to help capture inherent variability efficiently in a smaller space. A flattening approach leads to Euclidean spaces where dimension-reduction techniques such as PCA are available. Deng et al. (2021) used principal component analysis (PCA) to reach a low-dimensional vector-valued function space. While a spatial PCA reduces spatial dimension, the issue of high temporal dimensions (due to long sequences) remains. One can use techniques from functional analysis and fPCA (functional PCA) to control temporal dimensions. Alternatively, one can minimize spatio-temporal dimension jointly using tensor PCA. For instance, Lu et al. (2008) developed a multi-linear principal components analysis (MPCA) where higher-order tensor objects are iteratively unfolded into subspaces before applying standard PCA. Other tensor PCAs include Richard and Montanari (2014) and Huang et al. (2022).

Stochastic Models for Motion: After flattening \mathcal{Y} into a vector space, several ideas for stochastic process modeling become available. First, we can consider a discrete-time model. A classical model for (discrete) time-series data is the autoregressive model. Zhang et al. (2014) used the *autoregressive integrated moving average* (ARIMA) model to predict knee joint rotation. They viewed the rotation angles of the knee movements as separate scalar functions but did not consider the whole shape as a single object. Similarly, Wang et al. (2018) fitted an ARIMA model to predict the trajectories of arm movements. Deng et al. (2021) mapped 2D shapes into a Euclidean space, using TVF followed by a spatial PCA, and then used the *vector autoregressive* (VAR) model. One can use a more general Markov chain designed to capture human motions. Sidenbladh et al. (2002) used an implicit probabilistic model to generate the motion in discrete states with additive white noise. Gehrig et al. (2009) used a *hidden Markov model* (HMM) for action recognition, and Lehrmann et al. (2014) developed a nonlinear HMM modeling to analyze human motions. However, these methods generally fail to capture patterns in long sequences. In addition to the traditional statistical models, neural network methods provide another solution for simulating human motions. For example, *recurrent neural networks* have been used for predicting and simulating human motions (Guo et al. 2020, Pavllo et al. 2020), and *generalized regression neural networks* to simulate simple movements (Bataineh et al. 2016). However, these time series models only work well for predicting short-term repetitive movements. Simulating an extended sequence of several distinct actions using a time series model is difficult. Furthermore, the use of time-series models on nonlinear manifolds, especially for long sequences, remains undeveloped.

Human motion can also be viewed as a continuous time process on \mathcal{Y} . From this perspective, Amor et al. (2015) and Park et al. (2022) applied the TSRVF framework to classify and analyze the motion sequences. Some papers have used diffusion models (Rasul et al. 2021, Biloš et al. 2023), adding random noise to the observed functions and employing autoregressive recurrent neural network to denoise process. Yi et al. (2012) proposed a model for human motion by mapping manifold-valued curves to a single Euclidean tangent space and then used Brownian motion to model the flattened curves. Lyu et al. (2021) combined stochastic differential equations with an *adversarial network* (GAN) to generate human movements.

Evaluation Metrics: Besides choices for representations and modeling of shape sequences, we also need metrics for evaluating proposed solutions. The natural metrics for comparing the predicted sequences and the ground truth are mean squared error (MSE) or mean absolute error (MAE) (Wang et al. 2018, Xu et al. 2019). However, these methods only measure prediction errors but not test the underlying distributions. Rizzo and Székely (2010) introduced a non-parametric k -sample test for equal distributions using distance components (DISCO). Zhang et al. (2022) modified this DISCO test to compare distributions of different (static) shape populations. It uses pair-wise shape metrics and a permutation test to determine whether two samples are from the same population. Liu et al. (2022) proposed another non-parametric test using pair-wise distances and a generalized Wilcoxon rank-sum test. We will utilize Zhang et al. (2022)'s approach to evaluate proposed solutions, but one can also use other tests instead.

3. Background: Shape Representation and Sequence Registration

We view human motion as a time-indexed sequence of human postures. A posture, in turn, is a set of 3D coordinates of fixed pre-determined landmarks on the human body. In such motion analysis, one considers variables such as locations, body sizes, and execution rates as nuisance variables. Therefore, we wish data analysis to be invariant to these variables. Sec. 3.1 presents a mathematical representation of human posture invariant to location and size. Sec. 3.2 performs a temporal alignment of all sequences as a pre-processing step to remove the execution rate variability.

3.1. Skeletal Shape Representation

Let $\mathbf{X} \in \mathbb{R}^{n \times 3}$ be the matrix of 3D coordinates of n pre-determined landmarks on human body. These landmarks can also form a tree hierarchy, as shown in Fig. 1. For any landmark i , the relative coordinates based on its parent landmark j can be defined as $\tilde{\mathbf{x}}_i = \mathbf{x}_i - \mathbf{x}_n$ where $\mathbf{x}_i \in \mathbb{R}^3$ is the coordinate of the i th landmark. The posture data \mathbf{X} can be represented by the root location \mathbf{x}_n and the relative coordinates $\tilde{\mathbf{X}} = (\tilde{\mathbf{x}}_1, \tilde{\mathbf{x}}_2, \dots, \tilde{\mathbf{x}}_{n-1})$. The root location \mathbf{x}_n is discarded to make the data invariant to the location. We normalize each relative coordinate $\tilde{\mathbf{x}}_i$ as $\mathbf{y}_i = \frac{\tilde{\mathbf{x}}_i}{\|\tilde{\mathbf{x}}_i\|}$ to remove the effects of body size and proportions. The posture data represented by $\mathbf{Y} = (\mathbf{y}_1, \mathbf{y}_2, \dots, \mathbf{y}_{n-1})$ is now invariant to locations, body size, and body ratio.

The space of all postures is $\mathcal{Y} = \underbrace{\mathbb{S}^2 \times \mathbb{S}^2 \times \dots \times \mathbb{S}^2}_{(n-1) \text{ times}}$, where $\mathbb{S}^2 \in \mathbb{R}^3$ is a unit sphere. The unit sphere is a well-studied Riemannian manifold. The distance between any two postures $\mathbf{Y}, \mathbf{Z} \in \mathcal{Y}$ is defined as

$$d_{\mathcal{Y}}(\mathbf{Y}, \mathbf{Z}) = \sum_{i=1}^{n-1} d_{\mathbb{S}^2}(\mathbf{y}_i, \mathbf{z}_i), \quad (1)$$

where $\mathbf{y}_i, \mathbf{z}_i \in \mathbb{S}^2$ are the i th element of the corresponding postures \mathbf{Y} and \mathbf{Z} , and $d_{\mathbb{S}^2}(\mathbf{y}_i, \mathbf{z}_i) = \cos^{-1}(\mathbf{y}_i^\top \mathbf{z}_i)$ is the Riemannian distance on \mathbb{S}^2 .

Since the unit sphere \mathbb{S}^2 is non-linear, we perform statistical analysis on its tangent space, which is Euclidean. The tangent space of \mathcal{Y} at any $\mathbf{Y} \in \mathcal{Y}$ is defined elementwise as $T_{\mathbf{Y}}(\mathcal{Y}) = T_{\mathbf{y}_1}(\mathbb{S}^2) \times T_{\mathbf{y}_2}(\mathbb{S}^2) \times$

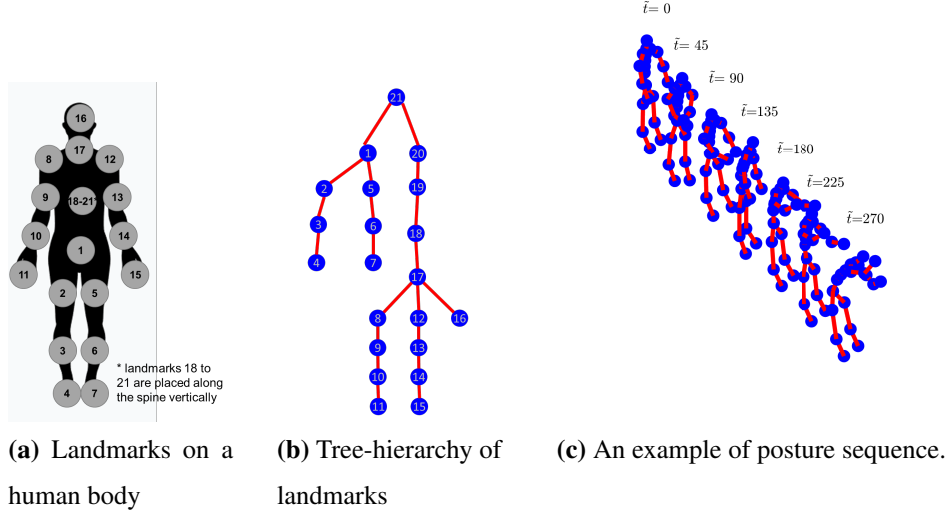


Figure 1 Illustration of landmarks on the human body.

$\dots \times T_{\mathbf{y}_{n-1}}(\mathbb{S}^2)$, where $T_{\mathbf{y}_i}(\mathbb{S}^2) = \{\mathbf{v} \in \mathbb{R}^3 | \mathbf{y}_i^\top \mathbf{v} = 0\}$ is the tangent space of the unit sphere at point \mathbf{y}_i . We can project any point $\mathbf{Z} \in \mathcal{Y}$ to the tangent space $T_{\mathcal{Y}}(\mathcal{Y})$ using the element-wise inverse exponential map

$$\exp_{\mathcal{Y}}^{-1}(\mathbf{Z}) = (\exp_{\mathbf{y}_1}^{-1}(\mathbf{z}_1), \exp_{\mathbf{y}_2}^{-1}(\mathbf{z}_2), \dots, \exp_{\mathbf{y}_{n-1}}^{-1}(\mathbf{z}_{n-1})), \quad (2)$$

where $\exp_{\mathbf{y}_i}^{-1}(\mathbf{z}_i)$ is the inverse exponential map on \mathbb{S}^2 . For any \mathbf{y}_i and $\mathbf{z}_i \in \mathbb{S}^2$, it is defined as $\exp_{\mathbf{y}_i}^{-1}(\mathbf{z}_i) = \frac{\theta_i}{\sin(\theta_i)}(\mathbf{z}_i - \mathbf{y}_i \cos(\theta_i))$ where $\theta_i = \cos^{-1}(\mathbf{y}_i^\top \mathbf{z}_i)$. The tangent space $T_{\mathbf{y}_i}(\mathbb{S}^2)$ is a 2D vector space and has an basis say $\{\mathbf{v}_{\mathbf{y}_i}, \mathbf{w}_{\mathbf{y}_i}\}$. Any tangent vector can be expressed as a vector $\mathbf{c}_i = (c_{i1}, c_{i2})^\top$ with respect to this basis. That is, $\exp_{\mathbf{y}_i}^{-1}(\mathbf{z}_i) = c_{i1}\mathbf{v}_{\mathbf{y}_i} + c_{i2}\mathbf{w}_{\mathbf{y}_i}$ and $\exp_{\mathcal{Y}}^{-1}(\mathbf{Z})$ becomes a $2 \times (n-1)$ matrix $\mathbf{C}_{\mathcal{Y}} = (\mathbf{c}_1, \mathbf{c}_2, \dots, \mathbf{c}_{n-1})$. In order to perform an element-wise analysis on these postures and tangent vectors, we use a vectorized representation to rewrite the coordinator matrix, $\mathbf{C}_{\mathcal{Y}} \in \mathbb{R}^{2 \times (n-1)}$, as $\tilde{\mathbf{C}}_{\mathcal{Y}} = \text{vec}(\mathbf{C}_{\mathcal{Y}}) \in \mathbb{R}^{2(n-1)}$. Similarly, we can define the element-wise exponential map that maps any point on the tangent space to the unit sphere. For a given point $\mathbf{u}_i \in T_{\mathbf{y}_i}(\mathbb{S}^2)$, the exponential map is given by $\exp_{\mathbf{y}_i}(\mathbf{u}_i) = \cos(\|\mathbf{u}_i\|)\mathbf{y}_i + \sin(\|\mathbf{u}_i\|)\frac{\mathbf{u}_i}{\|\mathbf{u}_i\|}$. For any point $\mathbf{U} \in T_{\mathcal{Y}}(\mathcal{Y})$, the exponential map is

$$\exp_{\mathcal{Y}}(\mathbf{U}) = (\exp_{\mathbf{y}_1}(\mathbf{u}_1), \exp_{\mathbf{y}_2}(\mathbf{u}_2), \dots, \exp_{\mathbf{y}_{n-1}}(\mathbf{u}_{n-1})). \quad (3)$$

We can also define a parallel transport in the manifold that transports a tangent vector $\mathbf{U} \in T_{\mathcal{Y}}(\mathcal{Y})$ to another tangent space $T_{\mathcal{Z}}(\mathcal{Y})$ along the geodesic. Similar to the inverse exponential and exponential maps, the parallel transport is defined element-wise. The parallel transport in \mathbb{S}^2 is defined as $\mathbf{v}_{\mathbf{y}_i \rightarrow \mathbf{z}_i} = \mathbf{u}_i - \frac{2\mathbf{u}_i^\top \mathbf{z}_i}{\|\mathbf{y}_i + \mathbf{z}_i\|^2}(\mathbf{y}_i + \mathbf{z}_i)$, where $\mathbf{y}_i, \mathbf{z}_i (\neq \mathbf{y}_i) \in \mathbb{S}^2$ and $\mathbf{u}_i \in T_{\mathbf{y}_i}(\mathbb{S}^2)$.

3.2. Temporal Alignment Based on S-TSRVF

A motion sequence is made up of a sequence of postures. Although each posture is invariant to location, body size, and body ratio, a posture sequence is indexed by time. This motion data has phase variability,

i.e., different sequences have different execution rates of activities. For example, Fig. 1 shows two identical posture sequences processed with actions performed at different rates. We need to separate the phase from the motion and focus on the motion itself.

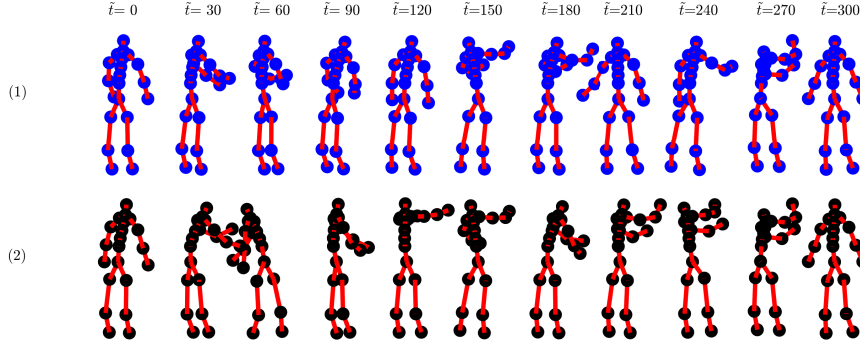


Figure 2 Two identical posture sequences with different execution rates. (1) and (2) are identical and sampled at every 30 postures. The misalignment is caused by different rates of execution.

We rescale the time period of individual sequences to the unit interval $[0, 1]$, and the posture sequence is expressed as a smooth map, $\alpha : [0, 1] \rightarrow \mathcal{Y}$. Let \mathcal{A} denote the space of all posture sequences, $\mathcal{A} = \{\alpha : [0, 1] \rightarrow \mathcal{Y}, \alpha \text{ is smooth}\}$. The distance between two posture sequences α_1 and α_2 can be defined as

$$d_{\mathcal{A}}(\alpha_1, \alpha_2) = \int_{[0,1]} d_{\mathcal{Y}}(\alpha_1(t), \alpha_2(t)) dt = \frac{1}{T} \sum_{t=1}^T d_{\mathcal{Y}}(\alpha_1(t), \alpha_2(t)). \quad (4)$$

We can time warp a posture sequence α by composing a function $\gamma : [0, 1] \rightarrow [0, 1]$ to assign a different time stamping according to $\alpha \mapsto \alpha \circ \gamma$. Here γ is a positive diffeomorphism of $[0, 1]$ to itself. The sequences α and $\alpha \circ \gamma$ contain the same postures but are reached at different time stamps, as shown in Fig. 2. Let Γ denote the set of all time-warping functions, $\Gamma = \{\gamma : [0,1] \rightarrow [0,1] | \gamma \text{ is a diffeomorphism, } \gamma(0) = 0, \gamma(1) = 1\}$. In order to remove phases from motion data, we define the motion of a sequence α by its equivalent class $[\alpha] = \{\alpha \circ \gamma \in \mathcal{A} | \gamma \in \Gamma\}$. The space of all motions becomes the quotient space \mathcal{A}/Γ .

To temporally align shape sequences, we represent them by the transported square-root vector field (TSRVF) with respect to a reference point $\mathbf{Y}_R \in \mathcal{Y}$. The TSRVF of a sequence α is given by, $h_{\alpha} : [0, 1] \rightarrow T_{\mathbf{Y}_R}(\mathcal{Y})$, where $h_{\alpha} = \frac{\dot{\alpha}(t)_{\alpha(t) \rightarrow \mathbf{Y}_R}}{\sqrt{\|\dot{\alpha}(t)\|}} \in T_{\mathbf{Y}_R}(\mathcal{Y})$, and where $\dot{\alpha}(t) = \exp_{\alpha(t)}^{-1}(\alpha(t+1)) \in T_{\alpha(t)}(\mathcal{Y})$ is the derivative of α (also called the *shooting vector*) at time t , and $\|\cdot\|$ is the Euclidean norm on the tangent space $T_{\alpha(t)}(\mathcal{Y})$. $\dot{\alpha}(t)_{\alpha(t) \rightarrow \mathbf{Y}_R}$ denotes the parallel transport of the shooting vector $\dot{\alpha}(t)$ from its original tangent space $T_{\alpha(t)}(\mathcal{Y})$ to the reference tangent space $T_{\mathbf{Y}_R}(\mathcal{Y})$ (along a geodesic in \mathcal{Y}). Due to a single hop needed in this transport, we sometimes call this the Single-Hop TSRVF or S-TSRVF. Let $\mathcal{H} = \{h_{\alpha} | \alpha \in \mathcal{A}\}$ be the space of S-TSRVFs. The S-TSRVF of a time warped shape sequence $\alpha \circ \gamma$ is $h_{\alpha \circ \gamma} = h_{\alpha}(\gamma(t)) \sqrt{\dot{\gamma}(t)}$. Define

a distance between any two S-TSRVFs h_{α_1} and h_{α_2} as $d_{\mathcal{H}}(h_{\alpha_1}, h_{\alpha_2}) = \int_0^1 \|h_{\alpha_1}(t) - h_{\alpha_2}(t)\| dt$. It can be shown that for any $\gamma \in \Gamma$, we have $d_{\mathcal{H}}(h_{\alpha_1}, h_{\alpha_2}) = d_{\mathcal{H}}(h_{\alpha_1 \circ \gamma}, h_{\alpha_2 \circ \gamma})$ (Su et al. 2014). Therefore, the distance between motion $[\alpha_1]$ and $[\alpha_2]$ is $d([\alpha_1], [\alpha_2]) = \min_{\gamma \in \Gamma} d_{\mathcal{H}}(h_{\alpha_1 \circ \gamma}, h_{\alpha_2 \circ \gamma})$. We can use dynamic programming to compute this distance along with an optimal time-warping function $\gamma^* = \arg \min_{\gamma \in \Gamma} (h_{\alpha_1 \circ \gamma}, h_{\alpha_2 \circ \gamma})$.

Given a reference sequence α_R , any motion sequence α can be aligned to α_R by solving for $\gamma_\alpha = \arg \min_{\gamma \in \Gamma} (h_{\alpha \circ \gamma}, h_{\alpha_R})$. As a result, all motion sequences are temporally aligned to the same reference sequence and thus synchronized. In this pre-processing way, we align given sequences and remove the temporal variability. From now on, we will assume that all the sequences are temporally aligned.

4. Mathematical Representations and Stochastic Modeling

In this section, we develop a pipeline for processing, modeling, and synthesizing human motion sequences from training data. The basic idea is to flatten the representation space \mathcal{Y} into a Euclidean space, reduce dimension using PCA-type tools, and impose analytical statistical models on synchronized, reduced representations. We then simulate novel sequences under this model and test their effectiveness in several ways, including visualizations and non-parametric two-sample tests.

Fig. 3 shows an outline of the proposed modeling pipeline. We start with given raw motion sequences and pre-align them using S-TSRVFs as described in the last section. The resulting aligned sequences, each discretized to length T , are now invariant to location, body size, body ratio, and execution rate. However, they are elements of a non-linear manifold $\mathcal{Y}^T = \underbrace{\mathcal{Y} \times \mathcal{Y} \times \dots \times \mathcal{Y}}_{T \text{ times}}$. The next step is to either flatten the sequences to a Euclidean space or model them as \mathcal{Y} -valued curves. After flattening, the next step is dimension reduction by spatial, temporal, or joint PCA. Then, we model the reduced representation using either a VAR model or a Gaussian process model. In the intrinsic approach, we use a simple point-wise Gaussian model to model manifold-valued curves directly. Finally, we generate random samples from these stochastic models and reconstruct new shape sequences. We describe these components next.

4.1. Mathematical Representation

This section discusses three representations of shape sequences: two methods that flatten the space into a Euclidean space and one that is intrinsic to the manifold.

1. Flattening Approach 1 – Integrated Single-Hop Transported Vector Field (IS-TVF): Instead of the S-TSRVF used in Sec. 3.2, we choose a different representation since the sequences are temporally aligned; we will call it *integrated single-hop transported vector field* (IS-TVF). The IS-TVF is inspired by the transported velocity field (TVF), which parallel transports the shooting vector along the path to a reference point. There are two transport schemes: (1) a single hop from the current point to a reference point and (2) multiple hops along the path to the starting point and then to a reference point. The multi-hop method accumulates significant numerical errors for longer sequences, creating considerable distortions. In contrast, a single-hop transport is numerically more accurate, although it may introduce a different distortion in the representation.

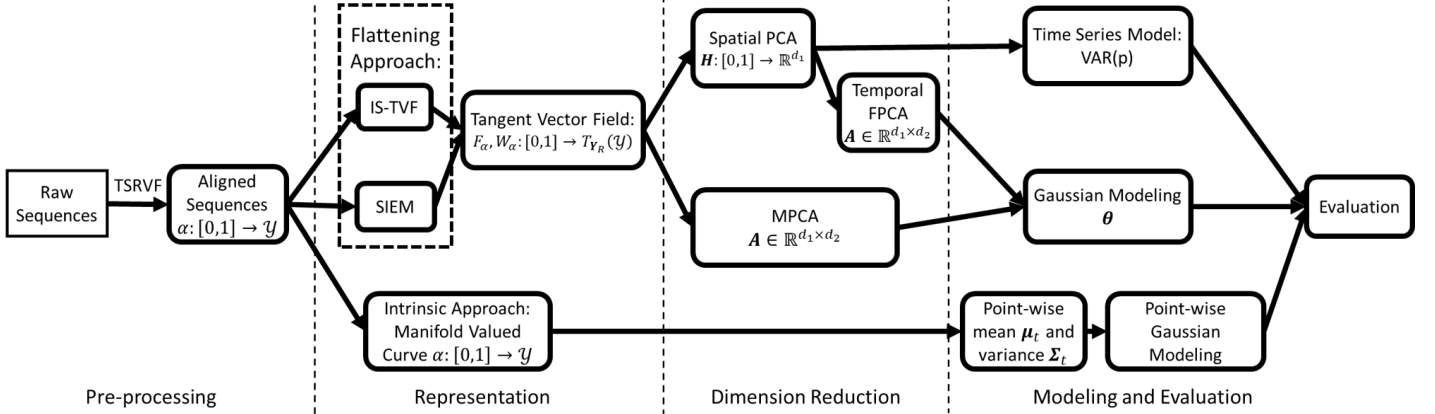


Figure 3 Pipeline for modeling motion sequences. The raw sequences are temporally aligned during the pre-processing, flattened into Euclidean time series, projected into small spaces using PCA, and then modeled using statistical models. One path follows a pointwise, intrinsic Gaussian (PWI) on the shape manifold directly. The pipeline is invertible: random quantities from statistical models on the right can be mapped back to full motion sequences.

DEFINITION 1. (Single-Hop TVF or S-TVF) For a sequence α , the single-hop transported velocity field (S-TVF) is defined as $\mathbf{F}_\alpha : [0, 1] \rightarrow T_{\mathbf{Y}_R}(\mathcal{Y})$ with $\mathbf{F}_\alpha(t) = \dot{\alpha}(t)_{\alpha(t) \rightarrow \mathbf{Y}_R} \in T_{\mathbf{Y}_R}(\mathcal{Y})$, where $\dot{\alpha}(t)_{\alpha(t) \rightarrow \mathbf{Y}_R}$ is the parallel transport of the shooting vector $\dot{\alpha}(t)$ from $T_{\alpha(t)}(\mathcal{Y})$ to $T_{\mathbf{Y}_R}(\mathcal{Y})$ along a geodesic.

Considering that we only have $T - 1$ shooting vectors for T time points, the S-TVF lies in $\mathbf{F}_\alpha \in \mathbb{R}^{3 \times (n-1) \times (T-1)}$ (recall that n is the number of landmarks on the body). The set $(\mathbf{Y}_R, \alpha(0), \mathbf{F}_\alpha)$ is a bijective map to α , which means that given the reference posture \mathbf{Y}_R , a starting posture $\alpha(0)$ and its corresponding S-TVF \mathbf{F}_α , the posture sequence could be reconstructed by the exponential map according to Eqn. 3: $\alpha(t) = \exp_{\alpha(t-1)}(\mathbf{F}_\alpha(t)_{\mathbf{Y}_R \rightarrow \alpha(t-1)})$, $t = 1, \dots, T - 1$. As a result, all the S-TVFs \mathbf{F}_{α_m} of different posture sequences α_m s are now in the same tangent space $T_{\mathbf{Y}_R}(\mathcal{Y})$. As mentioned in the Sec. 3.1, an element of $T_{\mathbf{Y}_R}(\mathcal{Y})$ can be expressed as a $2(n - 1)$ vector. Thus, an S-TVF sequence can be rewritten as $\mathbf{F}_{\alpha_m} \in \mathbb{R}^{2(n-1) \times (T-1)}$.

A practical challenge in using $\{\mathbf{F}_{\alpha_m}\}$ for analysis is that they represent velocities of the original motion, which could be sparse and noisy. To reach a denser and smoother representation, we utilize the integral of the S-TVF in practice; call it the *integrated* S-TVF (IS-TVF).

DEFINITION 2. (Integrated Single-Hop TVF) Given an S-TVF F_α , the integrated single-hop TVF (IS-TVF) is defined as $\mathbf{G}_\alpha : [0, 1] \rightarrow T_{\alpha(0)}(\mathcal{Y})$, where $\mathbf{G}_\alpha(t) = \int_0^t \mathbf{F}_\alpha(s) ds \approx \frac{1}{T-1} \sum_{s=1}^t \mathbf{F}_\alpha(s)$.

The IS-TVF represents positions rather than velocities of the motion sequence. Fig. 6a shows a cartoon illustration of the IS-TVF. The shooting vector $\dot{\alpha}(t)$ at time t is parallel transported to the tangent space of the starting point $\alpha(0)$ along a geodesic and then integrated to become a smooth curve on the tangent space. We can map IS-TVF back to S-TVF using finite differences. Both S-TVF and IS-TVF are $2(n - 1)$ -dimensional sequences with length $(T - 1)$, *i.e.*, $\mathbf{F}_\alpha, \mathbf{G}_\alpha \in \mathbb{R}^{2(n-1) \times (T-1)}$. Fig. 4 presents two examples

of S-TVF and IS-TVF of motion sequences. The S-TVF functions (in blue lines) appear sparse and noisy, while IS-TVF functions (in red lines) are much smoother.

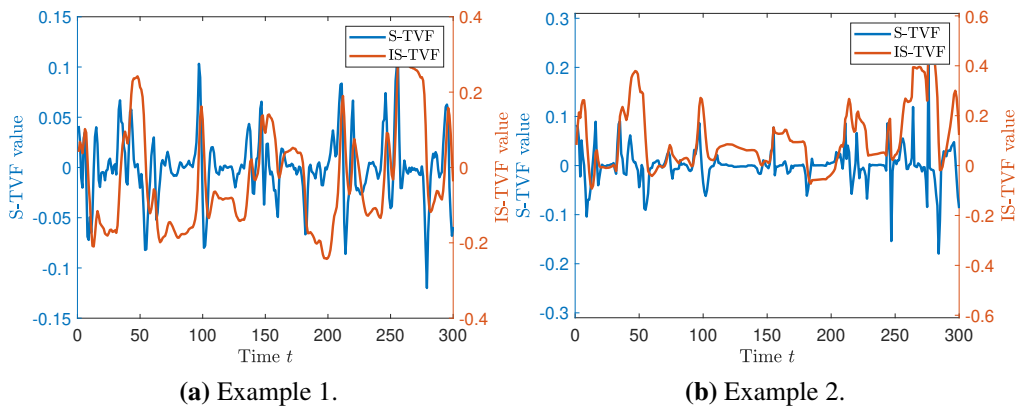


Figure 4 Examples of S-TVF (blue lines) and IS-TVF (red lines) of two motion sequences.

As mentioned above, S-TVF (and thus IS-TVF) is bijective. Given the starting point $\alpha(0)$ and IS-TVF \mathbf{G}_α , we reconstruct a posture sequence $\tilde{\alpha}$ using partial sums and parallel transports. Fig. 5a shows examples of reconstructions of a shape sequence from some of its flattened representations. The top row shows the original sequence, and the next three rows show reconstructions from S-TVF, M-TVF, and SIEM (Single Inverse Exponential Map). In these rows, the reconstructions (blue) are overlaid on the original sequences (black) to highlight the differences. Since IS-TVF and S-TVF curves overlap perfectly in this experiment, we have not drawn the former.

2. Flattening Approach 2 – Single Inverse Exponential Map (SIEM): Instead of using the shooting vectors of each step, the posture at time t , $\alpha(t)$, can be directly brought to the tangent space of a reference posture \mathbf{Y}_R by a single inverse exponential mapping (SIEM).

DEFINITION 3. (Single Inverse Exponential Map) The SIEM is defined as $\mathbf{W}_\alpha(t) = \exp_{\mathbf{Y}_R}^{-1}(\alpha(t))$, where $\alpha(t)$ is the human posture at time t and $\exp_{\mathbf{Y}_R}^{-1}(\cdot)$ is the inverse exponential map at the reference posture \mathbf{Y}_R (Eqn. 2).

SIEM is a bijective map locally, and we can invert the posture sequence using the exponential map $\alpha(t) = \exp_{\mathbf{Y}_R}(\mathbf{W}_\alpha(t))$ (Eqn. 3). Similar to the IS-TVF, $\mathbf{W}_\alpha(t)$ lies on the tangent space, $\mathbf{W}_\alpha \in \mathbb{R}^{2(n-1) \times T}$. \mathbf{W}_α is computationally simpler than the IS-TVF since it avoids computing velocity and integral. However, under SIEM, the distance between any two postures is not well preserved when the postures are far away from the reference posture. For example, Fig. 6b shows an illustration of the SIEM map, where the distance between two points on the manifold $\alpha(t_1), \alpha(t_2) \in \mathcal{Y}$, $d_{\mathcal{Y}}(\alpha(t_1), \alpha(t_2))$, is different from the distance of the corresponding points, $\mathbf{W}_\alpha(t_1), \mathbf{W}_\alpha(t_2) \in T_{\alpha(0)}(\mathcal{Y})$, on the tangent space. In contrast, the IS-TVF approach uses the velocity vectors $\dot{\alpha}(t)$ at each point (Fig. 6a), which better preserves distances between points during

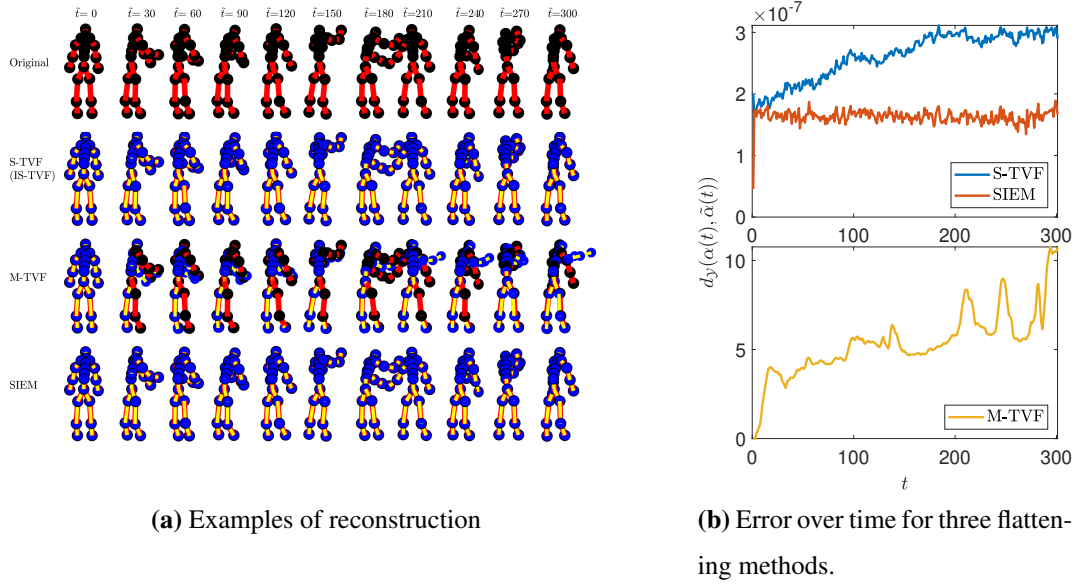


Figure 5 (a): Reconstruction examples of different flattening approaches. From top to bottom are: Original, S-TVF(IS-TVF), M-TVF, and SIEM. The black and red skeletons represent the actual observations, and the blue and yellow skeletons represent the reconstructed postures. The reconstructed and the original postures overlap for S-TVF and SIEM approaches because the numerical error is small. (b): Reconstruction error over time using S-TVF, SIEM, and M-TVF approaches. $e_{\mathcal{Y}}(t) = d_{\mathcal{Y}}(\alpha(t), \tilde{\alpha}(t))$ (Eqn. 1).

flattening since the length of the shooting vector $\dot{\alpha}(t)$ does not change during the parallel transport. Fig. 5a shows an example of the reconstruction. Similar to IS-TVF, the reconstructed sequences are identical to the original sequence. Fig. 5b shows the plots of reconstruction errors at each time to quantify the differences. The reconstruction error is defined as $e_{\mathcal{Y}} = d_{\mathcal{Y}}(\alpha(t), \tilde{\alpha}(t))$, where $d_{\mathcal{Y}}$ is the posture distance defined in Eqn. 1 and $\alpha(t)$ and $\tilde{\alpha}(t)$ are the original and reconstructed sequences at time t . S-TVF and SIEM, which use single-hop flattening, have stable and neglectable reconstruction errors around 10^{-7} , whereas the errors of M-TVF reconstruction accumulate significantly (up to 10).

3. Intrinsic Approach – Independent Shape-Valued Process: The posture sequence can also be studied as a \mathcal{Y} -valued process without flattening. However, performing statistical analysis on such a high-dimensional, nonlinear manifold is challenging. Given that the sequences are already temporally aligned, one can simplify by imposing an independent model at each time t . Furthermore, we can analyze them on the tangent space of the mean posture $\bar{\alpha}(t)$, $T_{\bar{\alpha}(t)}(\mathcal{Y})$. Since the postures at time t are often close to the mean $\bar{\alpha}(t)$, the distortion due to local flattening is smaller than the two flattening methods discussed earlier. The downside of this point-wise method is that it neglects the temporal relationship along the path. To incorporate spatial and temporal correlations in a \mathcal{Y} -valued process is considerably challenging. We will investigate the performances of the three ideas mentioned here.

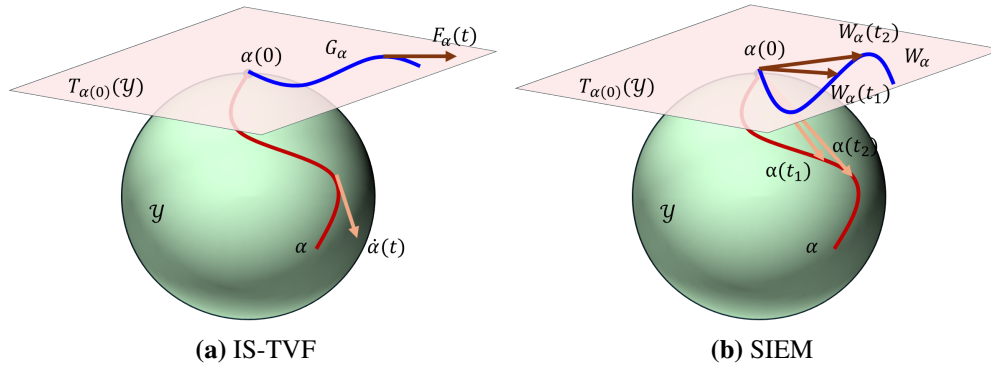


Figure 6 Cartoon Illustration of IS-TVF and SIEM. For IS-TVF, the velocity vectors at each time are transported to the tangent space of the reference point and then integrated to become trajectories on the tangent space. For SIEM, every point is directly mapped into a tangent space of a reference point. The pairs' distance between points on the manifold may be greatly distorted under SIEM flattening.

4.2. Space and Time Dimension Reduction

Both IS-TVF and SIEM are high-dimensional time series ($\mathbf{G}_\alpha \in \mathbb{R}^{2(n-1) \times (T-1)}$ and $\mathbf{W}_\alpha \in \mathbb{R}^{2(n-1) \times T}$), and it is necessary to apply some dimension-reduction techniques before statistical modeling. In the experiments presented here, we have $n = 21$ landmarks in a posture and a length of $T = 301$ for each sequence. Thus, the IS-TVF function has a spatial dimension of 40 and a temporal dimension of 300. The total spatio-temporal dimension of this data is $2(21 - 1) \times (301 - 1) = 12000$. We explore dimension reductions using PCA in the following sections. The first idea uses a sequential approach with a spatial principal component analysis (shape PCA), followed by a functional principal component analysis (FPCA). The second idea uses multilinear principal component analysis (MPCA) for joint spatio-temporal PCA.

Sequential Spatial and Temporal PCA: In this approach, the first step is spatial PCA, followed by temporal or FPCA. We will describe this process for IS-TVF, but the process is the same for SIEM. To reduce spatial dimensions of an IS-TVF sequence, $\mathbf{G}_\alpha \in \mathbb{R}^{2(n-1) \times (T-1)}$, we treat the vectors $\mathbf{G}_\alpha(t)$ for all α and t as points in $\mathbb{R}^{2(n-1)}$. For M sequences of length $T - 1$, the total number of the vector observations is $M(T - 1)$. We perform PCA of these vectors by computing the mean vector $\mathbf{m} = \frac{1}{M(T-1)} \sum_{i=1}^{M(T-1)} \mathbf{g}_i \in \mathbb{R}^{2(n-1)}$ and the covariance matrix $\Sigma = \frac{1}{M(T-1)-1} \sum_{i=1}^{M(T-1)} (\mathbf{g}_i - \mathbf{m})(\mathbf{g}_i - \mathbf{m})^\top \in \mathbb{R}^{2(n-1) \times 2(n-1)}$. Then, the SVD of the covariance matrix results in eigenvectors $\mathbf{u}_j \in \mathbb{R}^{2(n-1)}$. The resulting PCA projection matrix $\mathbf{U} \in \mathbb{R}^{2(n-1) \times d_1}$ is given by first (dominant) d_1 eigenvectors. Using this projection, each sequence \mathbf{G}_{α_m} can now be approximated by a d_1 -dimensional sequence $\mathbf{H}_{\alpha_m} \in \mathbb{R}^{d_1 \times (T-1)} = \mathbf{U}^\top \mathbf{G}_{\alpha_m}$. Given a coefficient sequence \mathbf{H}_{α_m} , the mean vector \mathbf{m} , and the projection matrix \mathbf{U} , one can reconstruct the IS-TVF sequence \mathbf{G}_{α_m} according to $\tilde{\mathbf{G}}_{\alpha_m}(t) = \mathbf{m} + \mathbf{U}\mathbf{H}_{\alpha_m}(t)$. Fig. 7 shows an example of this spatial PCA. It plots the eigenvalues and the first three PCA directions for motion data from one motion class. The bottom part of Fig. 7c is an example of some sequences reconstructed using the five spatial PCA components, *i.e.*, the spatial dimension is reduced from $2(n - 1) = 40$ to $d_1 = 5$.

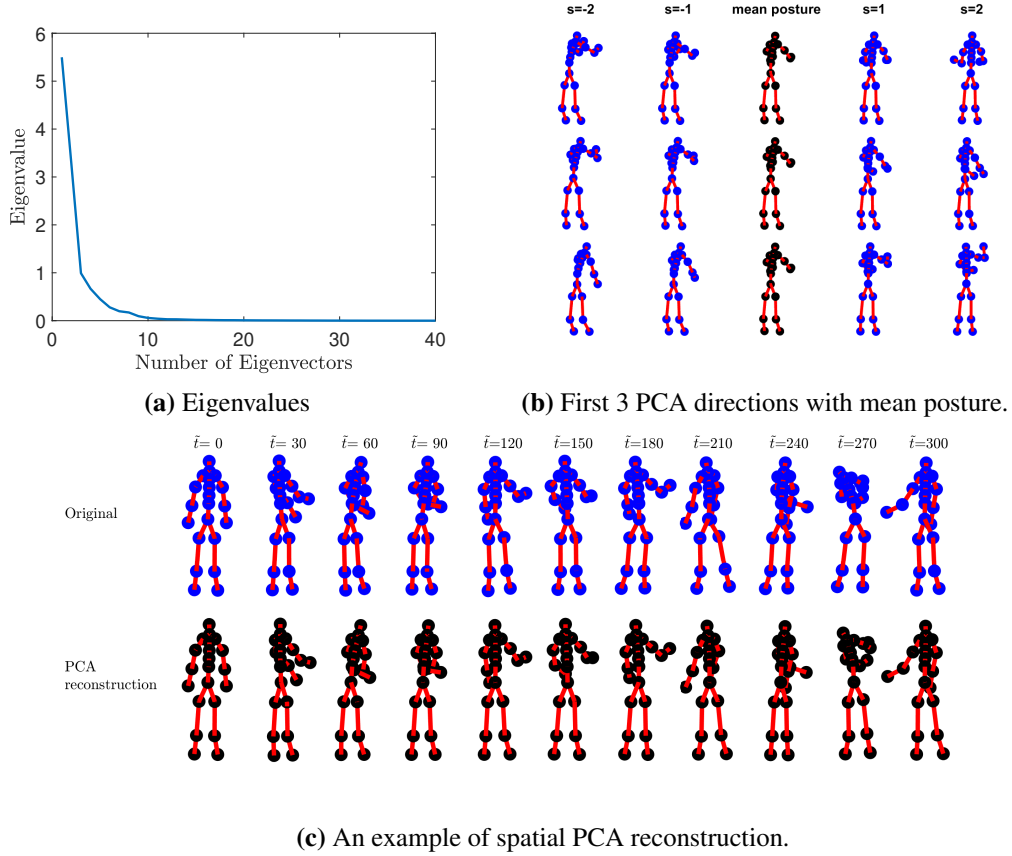


Figure 7 Results of spatial PCA using the first types of motion data we have. (a) is the plot of eigenvalues; (b) is the first 3 PCA directions; (c) is an example of spatial PCA reconstruction using the first five components with IS-TVF reconstructed motion for comparison (blue and red skeletons).

The spatial PCA reduces spatial dimension from $2(n - 1)$ to d_1 , but the temporal dimension $(T - 1)$ remains large. We view $\mathbf{H}_{\alpha_m}^{(i)}$, $i = 1, 2, 3, \dots, d_1$, $m = 1, 2, 3, \dots, M$ as scalar functions over an interval say $[0, 1]$, perform functional PCA on individual scalar-valued functions. We call it functional PCA for better interpretation, but in practice, this procedure performs PCA along T -length temporal *vectors*. For each scalar function $\mathbf{H}_{\alpha_m}^{(i)}$, we computed the functional mean $\boldsymbol{\mu}^{(i)} = \frac{1}{M} \sum_{m=1}^M \mathbf{H}_{\alpha_m}^{(i)} \in \mathbb{R}^{T-1}$ and the functional covariance $\boldsymbol{\Sigma}_f^{(i)} = \frac{1}{M-1} \sum_{m=1}^M \|\mathbf{H}_{\alpha_m}^{(i)} - \boldsymbol{\mu}^{(i)}\|^2 \in \mathbb{R}^{(T-1) \times (T-1)}$. Using eigen-decomposition of the covariance matrix, $\boldsymbol{\Sigma}_f^{(i)}$, we obtain eigenvectors $\boldsymbol{\beta}_k^{(i)}$ and eigenvalues $\lambda_k^{(i)}$. Fig. 7 shows the eigenvalues of the first spatial dimension $\mathbf{H}_{\alpha_m}^{(1)}$ as an example. Based on the largest d_2 eigenvalues, d_2 eigenvectors are selected as the basis functions. Accordingly, the individual scalar function $\mathbf{H}_{\alpha_m}^{(i)}$ can be approximated by $\tilde{\mathbf{H}}_{\alpha_m}^{(i)} = \boldsymbol{\mu}^{(i)} + \sum_{j=1}^{d_2} a_{ij} \boldsymbol{\beta}_j^{(i)}$, where $\boldsymbol{\mu}^{(i)}$ is the mean function for the i th dimension, $\boldsymbol{\beta}_j^{(i)}$ is the j th basis function for i th dimension, and a_{ij} is the corresponding coefficient of $\boldsymbol{\beta}_j^{(i)}$. The mean function and the first three basis functions of $\mathbf{H}_{\alpha_m}^{(1)}$ are shown in Fig. 7b as an example. Given a set of coefficients $\mathbf{A}_m = \{a_{ij}\}$, the sequence \mathbf{H}_{α_m} could be rebuilt by using corresponding mean $\boldsymbol{\mu}^{(i)}$, $i = 1, 2, \dots, d_1$ and basis functions $\boldsymbol{\beta}_j^{(i)}$, $i = 1, 2, \dots, d_1$, $j = 1, 2, \dots, d_2$. This step reduces the temporal dimension from $(T - 1) = 300$ to

$d_2 = 10$. Fig. 8c shows examples of the reconstructed scalar functions $\tilde{\mathbf{H}}_{\alpha_m}^{(i)}$, and Fig. 9a and Fig. 9b show examples of the reconstructed IS-TVF sequences $\tilde{\mathbf{G}}_{\alpha_m}^{(i)}$. The reconstructed posture sequence is slightly different from the original sequence, as shown in Fig. 9d due to the loss of details during dimension reduction. However, the main shape patterns are captured well for both PCA scalar functions $\mathbf{H}_{\alpha_m}^{(i)}$ and IS-TVF functions $\mathbf{G}_{\alpha_m}^{(i)}$. After performing the spatial and functional PCA, the dimension of the IS-TVF sequence is effectively reduced from $2(n-1) \times (T-1) = 12000$ to $d_1 \times d_2 = 5 \times 10 = 50$.

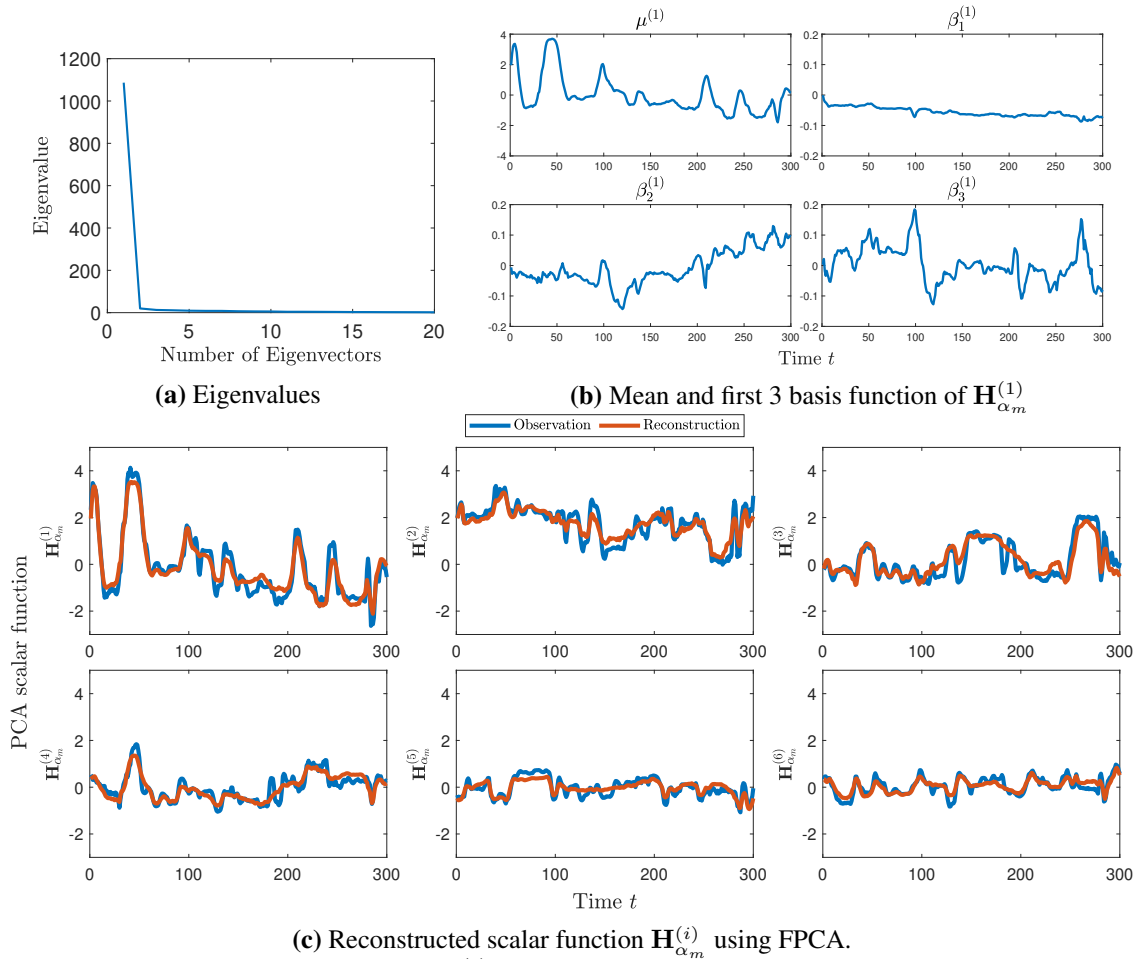
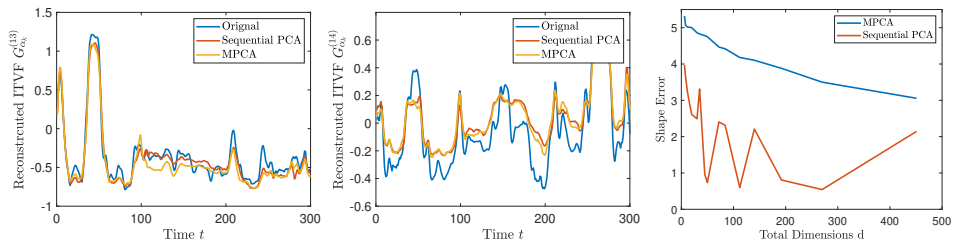


Figure 8 Results of FPCA for functional data $\{\mathbf{H}_{\alpha_m}^{(1)}\}$.

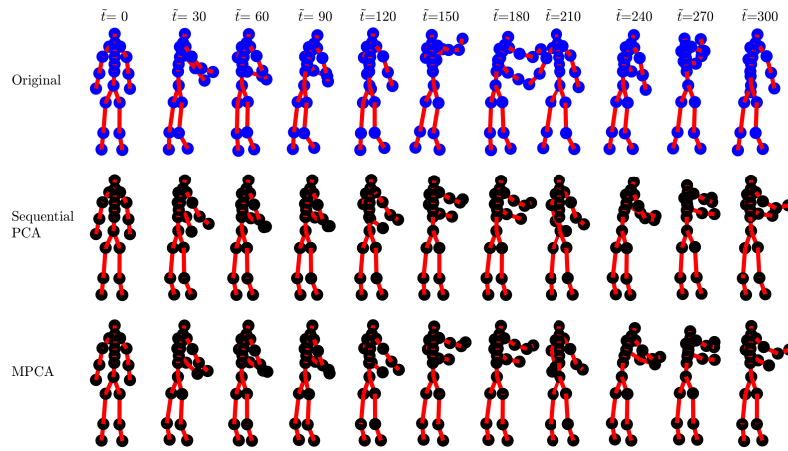
Joint Dimension Reduction: A more comprehensive albeit complex approach for dimension reduction is to reduce spatial and temporal dimensions simultaneously rather than sequentially. Here we view IS-TVF sequences \mathbf{G}_{α_m} (or SIEM \mathbf{W}_{α_m}) as a set of N th order tensors, $\{\mathcal{X}_m \in \mathbb{R}^{I_1 \times I_2 \times \dots \times I_N}, m = 1, 2, \dots, M\}$, in spatial and time dimensions. Then we apply the multilinear principal component analysis (MPCA) framework (Lu et al. 2008), essentially a tensor extension of the standard PCA. One can refer to Lu et al. (2008)'s paper for a detailed optimization algorithm. After the optimization, the feature tensor is obtained by a set of N projection matrices $\tilde{\mathbf{U}}^{(i)}$ as: $\mathcal{Z}_m = \mathcal{X}_m \times_1 \tilde{\mathbf{U}}^{(1)\top} \times_2 \tilde{\mathbf{U}}^{(2)\top} \times \dots \times_N \tilde{\mathbf{U}}^{(N)\top} \in \mathbb{R}^{d_1} \otimes \mathbb{R}^{d_2} \dots \otimes \mathbb{R}^{d_N}$,

where \times_s is the s -mode product, \otimes is the Kronecker product, and $d_s < I_s$ are the reduced dimensions. Conversely, the original tensor \mathcal{X}_m can be reconstructed by the features \mathcal{Z}_m as $\mathcal{X}_m = \mathcal{Z}_m \times_1 \tilde{\mathbf{U}}^{(1)} \times_2 \tilde{\mathbf{U}}^{(2)} \times \dots \times_N \tilde{\mathbf{U}}^{(N)}$.

The IS-TVF sequences $\mathbf{G}_{\alpha_m} \in \mathbb{R}^{2(n-1) \times (T-1)}$ (or SIEM \mathbf{W}_{α_m}) can be viewed as 2nd order tensor objects. As a result, we can obtain feature tensors $\mathcal{Z}_{\alpha_m} \in \mathbb{R}^{d_1} \otimes \mathbb{R}^{d_2}$ (with total dimension of $d_1 \times d_2 = 5 \times 4 = 20$ in this experiment), which is similar to the coefficient matrix $\mathbf{A}_k \in \mathbb{R}^{d_1 \times d_2}$ obtained by the sequential approach. Fig. 9 shows some example reconstructions of an element of the IS-TVF sequence $\tilde{\mathbf{G}}_{\alpha_m}^{(i)}$ from its PCA components. Similarly, Fig. 9d shows some reconstructed sequences from their PCA projections.



(a) Reconstructed example 1. (b) Reconstructed example 2. (c) Reconstruction error comparison.



(d) Examples of reconstruction.

Figure 9 Comparison of the MPCA and separate PCAs. (a) and (b) are examples of reconstructed IS-TVF elements. They are the same IS-TVF elements constructed by MPCA and sequential PCA. Both approaches provide a good approximation of the original functions. (c) is the reconstruction error versus the total reduced dimensions. The sequential PCA approach has a lower error when using the same reduced dimension d . (d) is the comparison between the reconstruction of sequential PCA and MPCA with the original sequence as a reference.

Performance Comparison Between the Joint and Sequential PCAs: In this section, we compare the performances of two PCA approaches in terms of dimension reduction and reconstruction error. We use the 85% total variance as the criterion for selecting d_1 and d_2 . In the sequential approach, we obtain $d_1 = 5$ to

retain 90% of the total spatial variance and $d_2 = 10$ for each spatial PCA dimension to cover 95% of the temporal variance. This results in $d_1 \times d_2 = 50$ total components. The joint PCA leads to 20 components (as a tensor matrix $\mathcal{Z}_m \in \mathbb{R}^{5 \times 4}$) as extracted by MPCA. Thus, MPCA is more effective than sequential PCA in reducing dimensions for the same retained variance.

However, the conclusions are reversed when comparing their reconstruction performances. The reconstructed IS-TVF functions (Fig. 9a and Fig. 9b) and posture sequences (as shown in Fig. 9d) are visually similar and reasonable with both methods. To quantify performance, we compare their reconstruction error defined as

$$e_{\mathcal{A}} = d_{\mathcal{A}}(\alpha_m, \tilde{\alpha}_m) \quad (5)$$

, where $d_{\mathcal{A}}$ is the sequence distance defined in Eqn. 4, and $\alpha_m, \tilde{\alpha}_m$ are the original and the PCA reconstructed sequences, respectively. The reconstruction error decreases faster using the sequential PCA approach as the PCA dimension increases, as shown in Fig. 9c. The spikes of the sequential PCA errors are caused by an inadequate number of spatial dimensions d_1 for certain selections of the total PCA dimension, , *e.g.*, $d_1 \times d_2 = 1 \times 41$ when setting the total PCA dimension as 41. As for MPCA, due to the consideration of the variation within each observation (*e.g.*, the variation between $\mathbf{G}_{\alpha_1}^{(1)}$ and $\mathbf{G}_{\alpha_1}^{(2)}$), which dominates the total variance, certain essential details for distinguishing different subjects, (*e.g.*, $\mathbf{G}_{\alpha_1}^{(1)}$, $\mathbf{G}_{\alpha_2}^{(1)}$, $\mathbf{G}_{\alpha_3}^{(1)}$, and *etc.*) are lost during the feature extraction, leading to poor reconstructions. Thus, we use the sequential method in the rest of this paper.

4.3. Statistical Modeling and Emulating Human Motion

After obtaining reduced Euclidean representations of motion sequences, we proceed to model them statistically to simulate new sequences.

4.3.1. Gaussian Models of PCA Coefficients We use $d = d_1 \times d_2$ scalar coefficients to represent each IS-TVF or SIEM sequence. Then, we use statistical models to fit the observed data. First, we study the empirical distributions of these coefficients using histograms of the training data. Fig. 10) shows these histograms with estimated Gaussian densities overlaid. These histograms motivate the use of Gaussian model $vec(\mathbf{A}) \sim N(\mathbf{0}, \Sigma)$, where $\Sigma \in \mathbb{R}^{d \times d}$ is estimated from the training data. We will call this multivariate Gaussian or simply MVG model. In case we use only the diagonal elements of Σ and discard off-diagonal elements, we get an independent Gaussian or IG model. In this experiment, we are limited by the amount of training data, leading to the relative instability of the estimated parameters. One can also impose a non-parametric model. However, the estimated non-parametric densities of the PCA coefficients are very close to the estimated Gaussian density, as shown in Fig. 10. Thus, we only use the Gaussian model in this paper.

Once a model is estimated, we can randomly sample a new set of coefficients \mathbf{A}^* from the estimated model. As discussed above, dimension reduction and flattening are bijective processes, and we can easily construct new posture sequences α^* from these random coefficients \mathbf{A}^* .

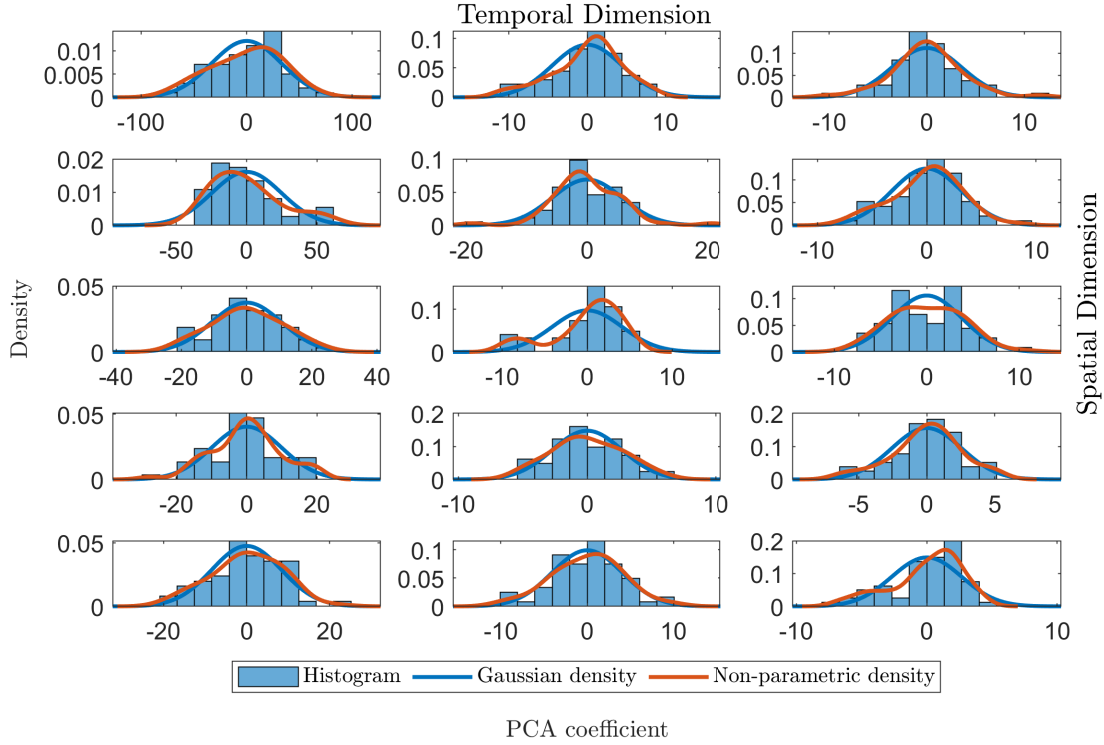


Figure 10 The histogram of coefficients obtained by sequential PCA using the motion data of the first motion class.

4.3.2. Time Series VAR Model Another classic approach for modeling a Euclidean sequence is a time-series model, such as the VAR (Vector Auto-Regressive) model (Hamilton 1994). We will investigate how well the VAR model fits the time-series data resulting from spatial PCA. That is, the motion sequence data are flattened by IS-TVF or SIEM, followed by a spatial PCA to obtain low dimensional vector-valued functions $\mathbf{H}_{\alpha_m} \in \mathbb{R}^{d_1 \times (T-1)}$. A VAR(p) model (of order p) is estimated using a randomly selected sequence as training data. We use $p = 12$ for these experiments. Then, we can simulate new sequences using the estimated model parameters. A similar simulation process is used in Deng et al. (2021)'s study.

4.3.3. Point-wise Intrinsic Independent Process (PWI) As mentioned earlier, there is also a possibility of modeling the human shapes on \mathcal{Y} without flattening. A straightforward approach for analyzing the manifold-valued curves is to use a point-wise Gaussian model; call it point-wise intrinsic (PWI) model. The point-wise (or cross-sectional) mean and covariance at each time $t \in [0, 1]$ can be estimated from the training data using:

$$\hat{\boldsymbol{\mu}}_{\mathcal{Y}}(t) = \arg \min_{\mathbf{Y} \in \mathcal{Y}} \sum_{m=1}^M d_{\mathcal{Y}}(\alpha_m(t), \mathbf{Y})^2, \quad \text{and} \quad \hat{\boldsymbol{\Sigma}}_{\mathcal{Y}}(t) = \frac{1}{M-1} \sum_{m=1}^M V_k(t) V_k(t)^\top, \quad (6)$$

where $d_{\mathcal{Y}}$ is the posture distance defined in Eqn. 1 and $V_k(t) = \exp_{\hat{\boldsymbol{\mu}}_{\mathcal{Y}}(t)}^{-1}(\alpha_m(t))$ is the shooting vector defined by the inverse exponential map in Eqn. 2. With the estimated model parameters, we can generate new sequences as follows. At each time t , we generate a random vector from an independent Gaussian

model $\mathbf{V}^*(t) \sim N(\boldsymbol{\mu}_y(t), \boldsymbol{\Sigma}_y(t))$ in the tangent space $T_y(\boldsymbol{\mu}_y(t))$. Then, we map this vector $\mathbf{V}^*(t)$ into a new posture $\alpha^*(t)$ using the exponential mapping defined in Eqn. 3, according to $\alpha^*(t) = \exp_{\boldsymbol{\mu}_y(t)}(\mathbf{V}^*(t))$. Note that this model assumes independence of $\alpha^*(t)$ from $\alpha^*(s)$ for $t \neq s$, which is a major limitation.

We will use the following convention to denote a scheme with choices of representation, dimension reduction, and statistical model:

$$\text{Scheme} = \text{Representation/DimensionReduction/StatisticalModel}.$$

For example, *IS-TVF/Sequential-PCA/MVG* denotes using IS-TVF flattening of sequences, Sequential PCA for dimensional reduction, and multivariate Gaussian for modeling the PCA coefficients. Similarly, *SIEM/Sequential-PCA/MVG* implies the same choices except the representation is now based on SIEM flattening; *SIEM/Sequential-PCA/IG* stands for an SIEM representation, Sequential PCA, and independent Gaussian models; *SIEM/Spatial-PCA/VAR* denotes SIEM representation, spatial PCA, and a VAR model.

4.4. Evaluation Metrics

After imposing a statistical model on reduced and simplified representations of motion sequences, we generate new random sequences from the learned models. The next question is: How are these random sequences statistically compared to real motion sequences? We will utilize several techniques for qualitative and quantitative evaluations. The qualitative approach is to visualize random sequences for visual inspections. The quantitative approaches include likelihood computations, hypothesis tests, and a quantization-based evaluation. More details of the quantitative approaches are described below:

1. **Log-likelihood:** One way to evaluate the simulated sequences α^* is to compute their log-likelihood under the statistical model estimated from the training data. One can compare the log-likelihoods of the simulated data with those of the original training data. Suppose that the estimated parameter from the original data is Θ . We can then compute the log-likelihood as:

$$\log L(\alpha^*|\Theta) = \log f(\mathbf{A}^*|\Theta) = \log\left\{(2\pi)^{\frac{d_1 d_2}{2}} \det(\boldsymbol{\Sigma})^{\frac{1}{2}} \exp\left(\frac{1}{2} \text{vec}(\mathbf{A}^*)^\top \boldsymbol{\Sigma}^{-1} \text{vec}(\mathbf{A}^*)\right)\right\}, \quad (7)$$

where \mathbf{A}^* is the simulated coefficients matrix, and f is the corresponding density function, which is the Gaussian density in this paper.

2. **Two-sample test:** For samples from two populations, we can perform a non-parametric DISCO test (Rizzo and Székely 2010) to compare whether the two samples are from the same probability distribution. Our experiment uses the training and the simulated sequences as these two samples. The test statistic is:

$$\epsilon(A, B) = \frac{2}{n_A n_B} \sum_{i=1}^{n_A} \sum_{j=1}^{n_B} d_{\mathcal{A}}(a_i, b_j) - \frac{1}{n_A^2} \sum_{i=1}^{n_A} \sum_{j=1}^{n_A} d_{\mathcal{A}}(a_i, a_j) - \frac{1}{n_B^2} \sum_{i=1}^{n_B} \sum_{j=1}^{n_B} d_{\mathcal{A}}(b_i, b_j),$$

where A and B are sets of the training and simulated sequences, with respective sample sizes n_A and n_B ; $d_{\mathcal{A}}(a, b)$ is the posture sequence distance defined in Eqn. 4.

The null hypothesis is that the distributions underlying the training and the generated data are the same, and the p -value is obtained from the permutation test (Liu et al. (2022)). One can refer to Rizzo and Székely (2010)'s paper for more details. $\epsilon(A, B)$ compares cross-group distances, $d(a_i, b_j)$, with the within-group distances, $d(a_i, a_j)$ and $d(b_i, b_j)$, to check equality of underlying distributions. Suppose the two samples are from different populations, as shown in Fig. 11a. In that case, the cross-group distances will be larger than the within-group distances, leading to a larger test statistic $\epsilon(A, B)$ and a smaller p value. This small p -value helps reject the claim that they are from the same population. On the other hand, when the two samples are close, as in Fig. 11b, the differences across groups are similar to distances within groups. The test statistic is small, and the p -value is large, failing to reject the null hypothesis.

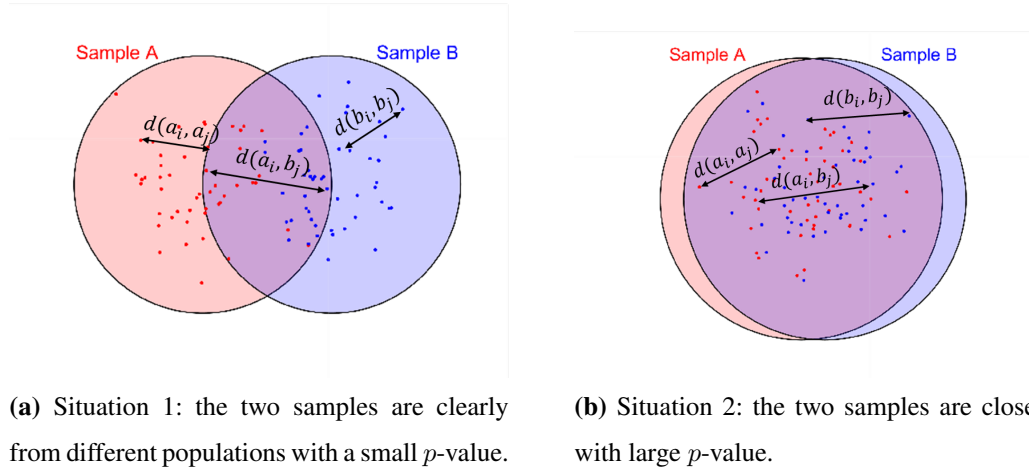


Figure 11 Pictorial illustration of the two-sample DISCO test.

3. Shape Quantization and Posture Evaluation: Another way to validate simulated motion sequences, especially in industrial settings, is to consider the underlying tasks performed by human workers. These tasks require the workers to go through preset sequences of postures (*e.g.*, lifting a part, walking to the station, etc.). One can use the appropriateness of postures to evaluate the simulated sequences. To implement this idea, we cluster all training postures ($\{\alpha_m(t), m = 1, \dots, M, t = 1, \dots, T\}$ s) into K disjoint groups. We then treat the cluster means $\{\mathbf{V}_k \in \mathcal{Y}, k = 1, \dots, K\}$ as *canonical postures* and *quantize* any given sequence into a time-series of cluster memberships. We use mode-based clustering of Deng et al. (2022) that requires pairwise shape distances between individual postures from training sequences. The algorithm automatically selects nine clusters using a random sample of 5,000 postures from the training data. Fig. 12a shows the sorted distance matrix after clustering, and Fig. 12b shows the cluster means or canonical postures. To quantize a sequence, we assign to each posture $\alpha_m(t)$ its nearest mode posture \mathbf{V}_k . Thus, a posture

sequence α_m is now a quantized (or label) sequence $\mathbf{B}_i(t) = b_t$, where $b_t \in \{1, 2, \dots, K\}$. Let $\bar{\mathbf{B}}$ denote the quantization of the mean sequence $\hat{\boldsymbol{\mu}}(t)$ (defined in Eqn. 6). Fig. 12c shows some examples of the individual quantized sequences and the quantized mean sequence.

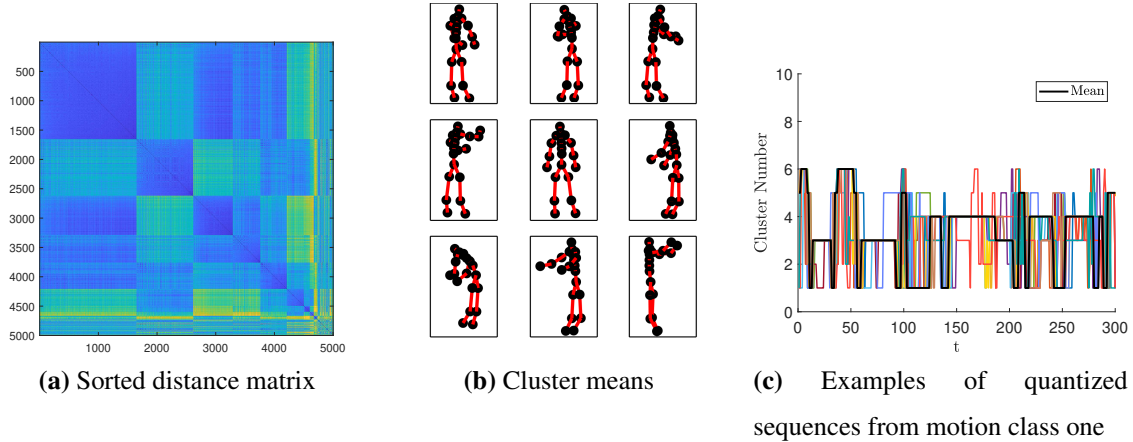


Figure 12 Example of the quantization of motion shapes into cluster labels. (a) shows the sorted distance matrix after clustering; (b) shows nine cluster-mean shapes for the posture data; (c) shows examples of quantized sequences \mathbf{B}_m (colored lines) with the quantized mean sequences $\bar{\mathbf{B}}$ (black lines) from one motion class.

The quantized mean sequence $\bar{\mathbf{B}}$ can be used as a reference sequence to check if an arbitrary sequence follows similar postures. The difference between a quantized sequence \mathbf{B}_i and the reference sequence $\bar{\mathbf{B}}$ can be measured using: $E(m) = \frac{1}{T} \sum_{t=1}^T \mathbf{1}_{\mathbf{B}_m(t) \neq \bar{\mathbf{B}}(t)}$. We can further compute the mean and variance of the variability of $E(m)$, call them \bar{E} and $Var(E)$, over many simulated sequences, to evaluate simulations.

In addition to studying cluster-label sequences, we also compute cluster transition matrices from quantized sequences to evaluate if the simulated sequences capture the trend of the motion. Since long motion sequences are not stationary over time, they can't be described by a single transition matrix. Instead, the transition matrices are estimated over a sliding time window of size l , $[t_0, t_0 + l]$, and stepsize δ_l . That is, the next window is $[t_0 + \delta_l, t_0 + \delta_l + l]$. As a result, we can obtain a sequence of transition matrices $\mathbf{Q} = \{\mathbf{Q}(t), t = 0, \delta_l, 2\delta_l, \dots\}$. The elements of a transition matrix $\hat{\mathbf{Q}}(t)$ at time t are estimated as $\hat{q}_{ij}(t) = \frac{\sum_{m=1}^M \sum_{s=t}^{t+l} \mathbf{1}_{(\mathbf{B}_m(s)=i, \mathbf{B}_m(s+1)=j)}}$, where i, j are the cluster means. We use the L^1 norm to measure the differences between the transition matrices for training, $\hat{\mathbf{Q}}$, and simulated sequences, \mathbf{Q}^* . A uniform transition matrix, *i.e.*, $\hat{q}_{ij}(t) = \frac{1}{K}$, is also created as a random walk scenario to compare against.

5. Experiment Results and Evaluation

This section presents comprehensive results on imposing and estimating statistical models from sequence data and simulating novel human motions from these models. We also provide exhaustive evaluations of different approaches and draw conclusions about the performance of this pipeline.

5.1. Data Description and PCA Dimensions

Data Description and PreProcessing: The human motion sequence data used in this study is collected in an industrial setting. Each motion sequence records a worker performing a task over time at their workstation. The dataset includes five motion classes, with 60 sequences for each class, *i.e.*, 300 total motion sequences. The skeletons have $n = 21$ landmarks each, so $\alpha(t)$ has $3 \times (21 - 1) = 60$ dimensions at each t . The sequences are sampled at $T = 1000$ time points. However, some activities are limited to subtle movements and minor shape changes over long periods. Hence, we down-sampled the sequences to 301 time points to help reduce redundancy and bring down the computational cost. These sequences were temporally aligned using pre-processing described in Sec. 3.2.

Choosing PCA Dimensions: We must first choose appropriate dimensions d_1 and d_2 for spatial and temporal PCAs. We select them using two criteria: (1) minimize reconstruction error in Eqn. 5 and (2) pass the two-sample test between the original and the reconstructed sequences. Fig. 13a shows the reconstruction errors versus d_2 (for $d_1 = 5$ and 10), and Fig. 13b shows the mesh plot of reconstruction error over d_1 and d_2 . Increasing d_1 seems more effective in terms of reducing the reconstruction error. Hence, we chose $d_1 = 10$. Then, we performed the two-sample test between the original and the reconstructed sequences to confirm that these two sets of sequences are from the same distribution. Fig. 13c shows the p -values of the two-sample test versus d_2 values. Accordingly, we selected $d_2 = 30$.

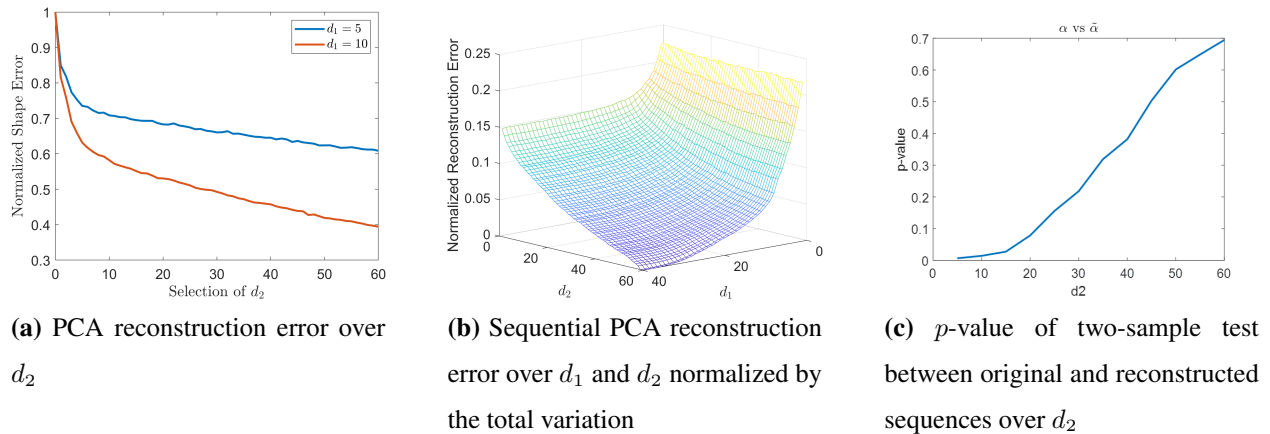


Figure 13 PCA reconstruction experiment. The left is the reconstruction error defined in Sec. 4.2 over different d_2 when $d_1 = 5$ and 10. The middle is the mesh plot of the reconstruction error over d_1 and d_2 . The right is the p -value of the two-sample test over d_2 when d_1 is fixed at 10.

5.2. Evaluating Sub-sequences of Simulated Sequences

Due to the limited nature of our dataset (we have only 60 observed sequences per each motion class), analyzing performance on 300-length sequences is challenging. This is because the number of model parameters

far exceeds the data available for estimating them. Therefore, we restrict ourselves to smaller sub-sequences to limit the number of PCA coefficients representing motion data. Tab. 1 provides a listing of which sub-sequences have been used. Then, we chose spatial PCA and FPCA dimensions for selected sub-sequences, as discussed previously. Tab. 1 also lists chosen PCA dimensions and the mean PCA reconstruction errors (Eqn. 5) for two representations: IS-TVF and SIEM. In most cases, reconstruction errors using SIEM are smaller than those using IS-TVF because SIEM does not require differentiating and integrating steps that can potentially cause numerical errors. This section mainly uses sub-sequences, $\{\alpha'_i\}$, from $t = 180$ to 240 of the observed sequences since the sub-sequences contain many representative movements. We then apply sequential PCA with $d_1 \times d_2 = 8 \times 4$ as illustrated in Tab. 1 and use several different statistical models discussed in Sec. 4.3 to simulate new sub-sequences $\{\alpha_i^*\}$. Finally, we compare the simulated sub-sequences $\{\alpha_i^*\}$ with $\{\alpha'_i\}$ using visualization, MDS analysis, two-sample test, and smoothness evaluation.

Sub-sequences	Reduced Dimension ($d_1 \times d_2$)	Reconstruction Error	
		IS-TVF/PCA	SIEM/PCA
Subsequence 180-210	8×4	1.5353	1.7289
Subsequence 180-240	10×5	2.2388	2.0425
Subsequence 180-300	12×10	2.4576	1.9313

Table 1 Dimension selection and mean reconstruction errors (as described in Sec. 4.2) of sequential PCA using IS-TVF and SIEM on sub-sequences.

Visual Comparisons: Fig. 14 shows simulated sub-sequences from the first motion class using different modeling methods developed earlier. The *IS-TVF/SequentialPCA/MVG* and *SIEM/SequentialPCA/MVG* approaches simulate realistic sequences by retaining broad spatial and temporal patterns. The PWI model ignores the temporal correlations in sequences, and, as a result, the sequences lack temporal structure. The shapes are essentially independent samples around their means without any connection between successive shapes. The *IS-TVF/SpatialPCA/VAR* model fails to capture the changing dynamics of body shapes. Therefore, the simulated postures keep deforming the same way until they become unrealistic. Perhaps a time-varying VAR model will perform better for the current application since it involves shape evolution over long periods.

MDS-Based Analysis of Simulated Data: In addition to visualizations of simulated sub-sequences, we compute MDS plots using $d_{\mathcal{A}}$ (defined in Eqn. 4) between training and simulated sequences. Fig. 15 shows the MDS plots of such data for different combinations of representations and models, with the red dots representing training sequences and the blue dots representing the simulated ones. As shown in the figure, the sequences simulated by the proposed *IS-TVF/SequentialPCA/MVG* and *SIEM/SequentialPCA/MVG* methods are distributed comparably to the training sequences. In contrast, the sequences simulated by the PWI model are close to the center without any meaningful variation, and the sequences by the *IS-TVF/SpatialPCA/VAR* model lie far away from the original sequences.

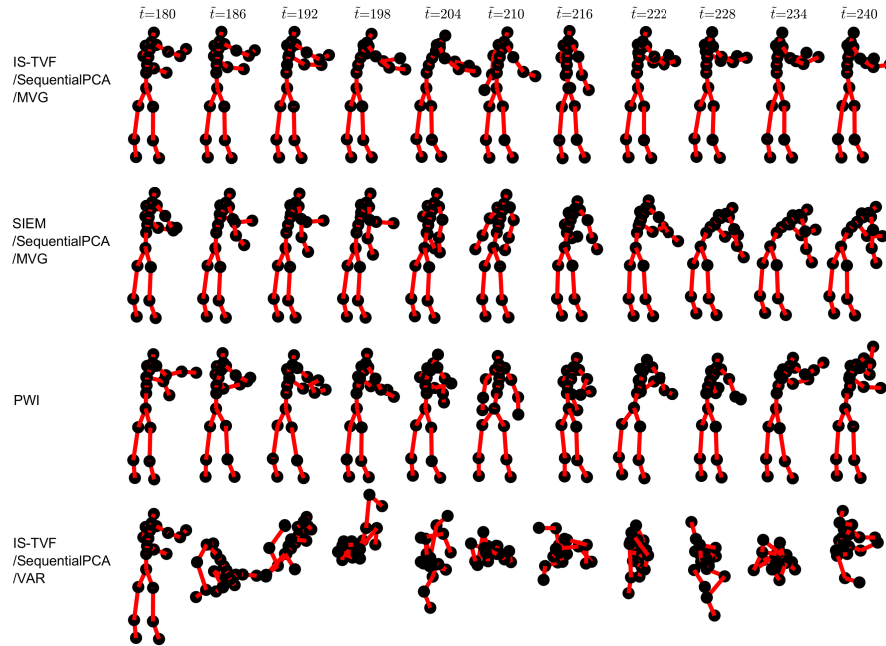


Figure 14 Simulated sub-sequences from $t = 180$ to 240 of motion class one simulated by different methods. From top to bottom: *IS-TVF/SequentialPCA/MVG*, *SIEM/SequentialPCA/MVG*, *PWI*, *IS-TVF/SpatialPCA/VAR*.

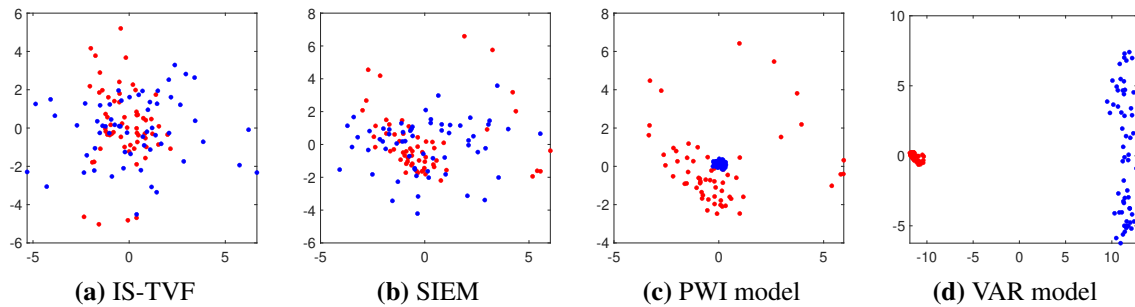


Figure 15 MDS plots of original $\{\alpha'_i\}$ and simulated sub-sequences $\{\alpha_i^*\}$. Red points are original sub-sequences, and blue points are simulated data. MDS was computed for each plot for its own set of sequences.

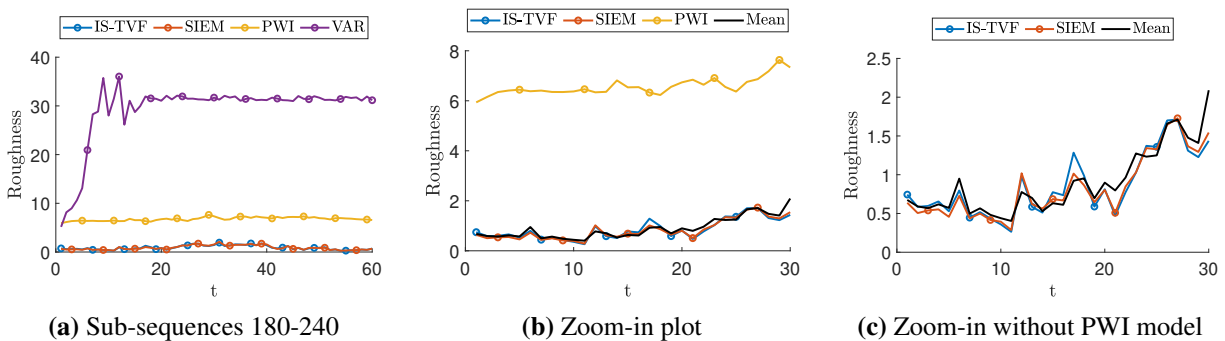


Figure 16 Plots of $d_y(\alpha(t), \alpha(t+1))$ versus t , $t \in [180, 240]$, for simulated sub-sequences under different models. The right two show zoom-ins and compare with the mean smoothness of the original sequences (black lines).

Two-sample Test for Comparing Populations: We also apply the two-sample test mentioned earlier (refer to Sec. 4.4) to check if the training and the simulated sequences are from the same distribution. Tab. 2 shows the p -value of the two-sample tests for different models. A small p -value will suggest that the simulated sequences differ from the training sequences in distribution. Thus, we prefer larger p values to underscore the success in capturing training distributions when simulating new sequences. In most situations, the sequences simulated by the *SIEM/SequentialPCA/MVG* model yield the best results, although the p -values were still small.

Sub-sequences	<i>IS-TVF/SequentialPCA/MVG</i>	<i>SIEM/SequentialPCA/MVG</i>	PWI	<i>IS-TVF/SpatialPCA/VAR</i>
180-210	0.0211	0.0544	0.0021	0
180-240	0.0109	0.0190	0.0011	0
180-300	0.0012	0.0022	0.0005	0

Table 2 p -values of two-sample tests on the different sub-sequences. The tests compare the 60 original $\{\alpha'_i\}$ and 60 simulated sub-sequences $\{\alpha_i^*\}$. This table shows the results for motion class one. The results for other motion classes are similar.

Evaluation Smoothness of Simulated Sequences: The original motion sequences are usually smooth as human workers cannot change postures rapidly. We expect the simulated motion sequences to be smooth. To evaluate the smoothness of the simulated motion sequences, we compute the temporal roughness of the simulated sequences as an evaluation criterion. Specifically, we use the shape differences between successive postures, $d_y(\alpha(t), \alpha(t+1))$ (with d_y given in Eqn. 1), as a measure of roughness. Fig. 16a shows a plot of this quantity versus t for simulated sub-sequences. Fig. 16b shows a zoom-in to highlight the differences between the proposed models and the PWI model, and Fig. 16c removes the PWI model to focus on the two flattening-based models. As these plots show, the two flattening models have smoother temporal evolution, similar to the original sequences. In contrast, the sequences from the PWI model are much rougher due to a lack of temporal relationships; see Fig. 16b. PWI sequences fluctuate around the mean sequence, which is unrealistic for operating motions. The *IS-TVF/SpatialPCA/VAR* model fails to capture the movements of the long sequences that contain several more minor activities. Thus, the simulated sub-sequence makes the same constant changes throughout the simulation process, yielding high temporal roughness.

5.3. Further Simulation and Testing from the Simulated Data

The goal of this paper is to simulate new, random sequences using models learned from the training data. Given the limited amount of real data available for evaluation, we employ a simulation study that allows us to generate as much data as necessary. Specifically, we use 60 observed sequences to fit a simple motion simulation model and then employ this fitted model to generate simulated datasets, which we refer to as the level-one simulation. Using these simulated datasets, we evaluate different statistical emulators.

As outlined in Fig. 17, the level-one simulation generates the necessary simulation data. Since the PWI model and VAR model do not perform well, as discussed in Sec. 5.2, we use *IS-TVF/SequentialPCA/IG* and

SIEM/SequentialPCA/IG models (with PCA dimension $d_1 \times d_2 = 5 \times 4$) for the level-one simulation. Each of the two models is fitted to the 60 observed sequences for the first motion class, and the fitted model is used to generate randomly 1,000 new sequences $\{\tilde{\alpha}_i\}$. We randomly divide them into a training set (800 sequences) and a test set (200 sequences).

Subsequently, we use the training set and test set as benchmark datasets to evaluate different statistical emulators, including the PWI model, *IS-TVF/SequentialPCA/MVG*, *IS-TVF/SequentialPCA/IG*, *SIEM/SequentialPCA/MVG*, and *SIEM/SequentialPCA/IG* models, all with PCA dimension $d_1 \times d_2 = 4 \times 4$. Each statistical emulator is fitted using the training set of the benchmark dataset, and the fitted emulator is used to simulate 200 sequences $\{\hat{\alpha}_i\}$, which we refer to as the level-two simulation data. The level-two simulated sequences $\{\hat{\alpha}_i\}$ are compared to the test set of the benchmark dataset, using log-likelihood and two-sample test mentioned in Sec. 4.4.

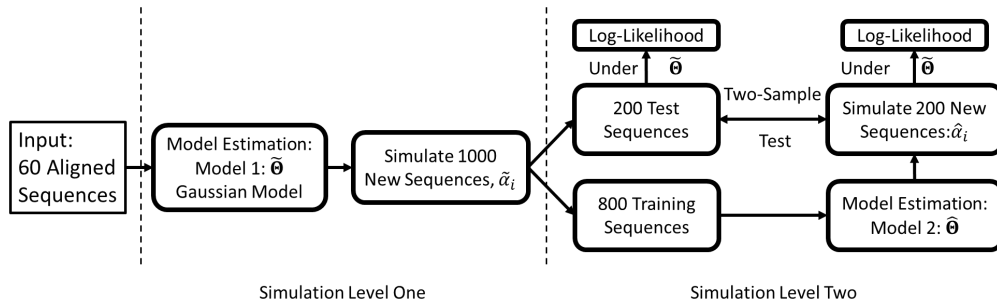
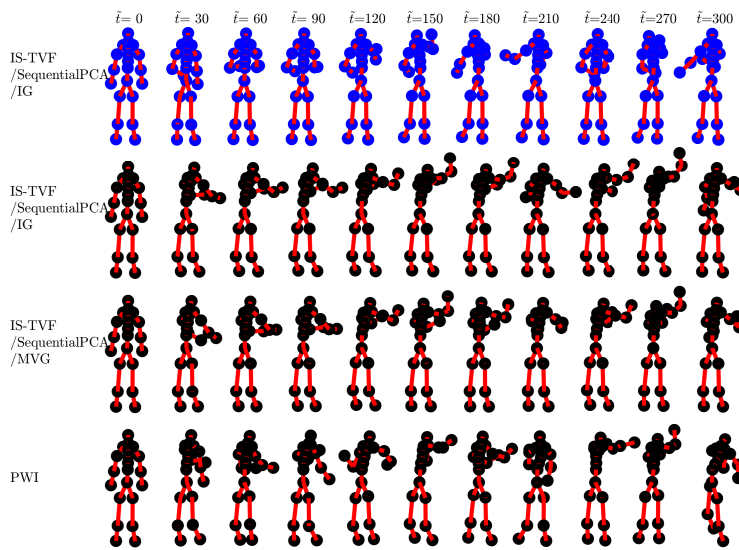


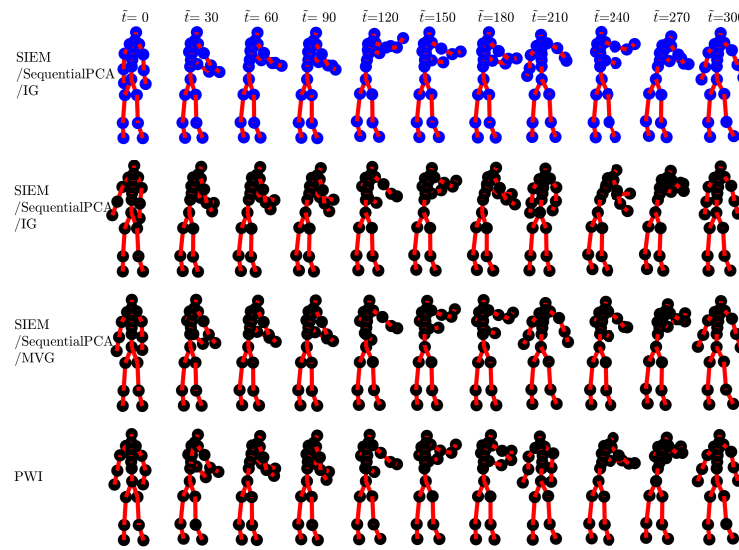
Figure 17 Simulation process. The first level simulation includes estimating a simple model $\tilde{\Theta}$ from the 60 pre-aligned sequences and simulating 1000 new sequences $\{\tilde{\alpha}_i\}$, which are treated as the ground truth for the simulation level two. The second level simulation estimates another model $\hat{\Theta}$ and simulates 200 sequences $\{\hat{\alpha}_i\}$ from the training set using $\{\tilde{\alpha}_i\}$. These 200 further simulated sequences $\{\hat{\alpha}_i\}$ are compared to the test sequences from the first simulation $\{\tilde{\alpha}_i\}$ using visual inspection, log-likelihood, and two-sample test mentioned in Sec. 4.4.

Visual Inspections of Level-Two Simulations: Fig. 18 shows some examples of the two-level simulation $\{\tilde{\alpha}_i\}$ and $\{\hat{\alpha}_i\}$. Fig. 18a uses *IS-TVF/SequentialPCA/IG* for the level-one simulation, and Fig. 18b uses *SIEM/SequentialPCA/IG* for the level-one simulation. Similar to the visual comparisons of the sub-sequences experiments (Sec. 5.1), the simulated sequences from the proposed models are realistic and reasonable compared to the benchmark training data.

Two-sample test: Besides visualization, we also use a two-sample test (Sec. 4.4) to compare a sample of 200 sequences in the benchmark test dataset versus a sample of 200 sequences simulated by statistical emulators. Tab. 3 shows the p -value of the two-sample tests for various simulated configurations. When the benchmark data is generated by the *IS-TVF/sequentialPCA/IG* model, the statistical emulators



(a) Simulation level one: *IS-TVF/SequentialPCA/IG*



(b) Simulation level one: *SIEM/SequentialPCA/IG*

Figure 18 Examples of the two level simulation $\tilde{\alpha}_i$ and $\hat{\alpha}_i$. The first row (black) is the level one simulation $\tilde{\alpha}_i$ using *IS-TVF/SequentialPCA/IG* and *SIEM/SequentialPCA/IG*. The rest of the rows are different models of simulation level two.

with *IS-TVF/sequentialPCA/MVG* model have the highest p -values in most of the simulation configurations. The p -values are significantly higher than popular statistical significance levels such as 0.01 or 0.05. This implies that the sequences emulated by the proposed *IS-TVF/sequentialPCA/MVG* emulators and *IS-*

TVF/sequentialPCA/IG emulators are distributed equally as the benchmark data with a high statistical significance level.

When the benchmark dataset is generated by the *IS-TVf/sequentialPCA/IG* model, the highest p -value was obtained by the *SIEM/sequentialPCA/IG* emulator. The p -values are again significantly higher than popular statistical significance levels such as 0.01 or 0.05.

Level One Model →	<i>IS-TVf/SequentialPCA/IG</i>			<i>SIEM/SequentialPCA/IG</i>		
Level Two Model →	<i>IS-TVf/SequentialPCA/IG</i>	<i>IS-TVf/SequentialPCA/MVG</i>	PWI	<i>SIEM/SequentialPCA/IG</i>	<i>SIEM/SequentialPCA/MVG</i>	PWI
Motion 1	0.6957	0.7192	0.2738	0.0451	0.0332	0.0010
Motion 2	0.3828	0.3650	0.1557	0.0256	0.0424	0.4499
Motion 3	0.5216	0.5867	0.1228	0.3571	0.0734	0.2418
Motion 4	0.8232	0.4073	0.1424	0.1647	0.0952	0.1169
Motion 5	0.3762	0.5085	0.2022	0.4208	0.1485	0.0201

Table 3 p -values of the two-sample tests on the two-level simulation. The first simulation uses *IS-TVf/SequentialPCA/IG* (left side) and *SIEM/SequentialPCA/IG* (right side). The models for simulation level two include IG and MVG with corresponding flattening methods (IS-TVf or SIEM) as well as PWI.

Q-Q Plot of Likelihood: Fig. 19 shows the Q-Q plots of the likelihood of the further simulated sequences compared with those of the test benchmark sequences, where the likelihood is calculated using Eqn. 7. As for the *IS-TVf/SequentialPCA/IG* experiments (the left plot of Fig. 19), the sequences simulated by different models perform similarly and follow the identity line except for the PWI model. The likelihood of the PWI model-simulated sequences is too small, so it is not visible in these charts. The results of *SIEM/SequentialPCA/IG* experiments (the right plot of Fig. 19) are similar. Both flattening approaches outperform the PWI model. The PWI model is closer to the ground truth than those in the *IS-TVf/SequentialPCA/IG* experiments but still performs the worst and does not follow the identity line. In terms of likelihood, the proposed models work well for modeling and simulating using the training data.

5.4. Evaluation Using Quantization

We also perform the evaluation using quantization as discussed in Sec. 4.4. There are 90,300 individual postures in total from all the five motion classes. We randomly selected a sample of 5,000 postures for computational efficiency. We get nine clusters for the 5,000 postures, as shown in Fig. 12b. Based on the clustering, each of the 5,000 motion sequences is quantized into a sequence of posture cluster numbers, which is referred to as a quantized sequence. We also apply the same quantization for the simulation sequences, which are simulated by the proposed emulators *IS-TVf/SequentialPCA/MVG* and *SIEM/SequentialPCA/MVG*, as well as the PWI model.

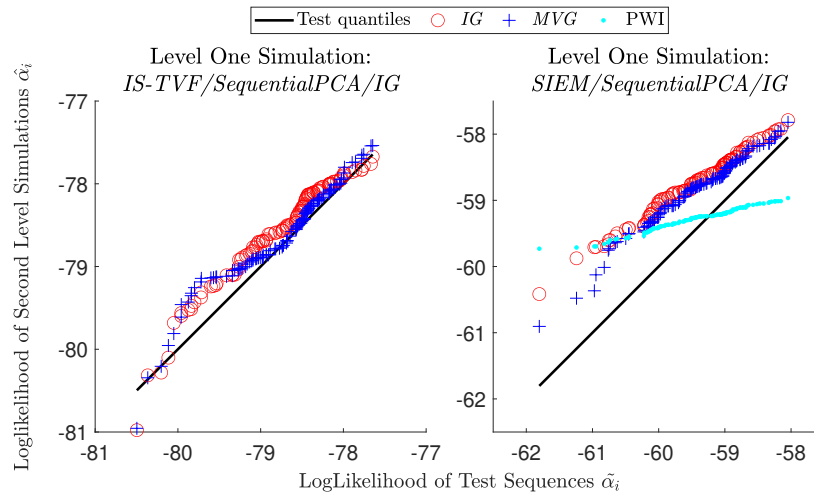


Figure 19 Q-Q plots of the sequences $\{\hat{\alpha}_i\}$ of level two simulation compared to the test data from the first simulation $\{\tilde{\alpha}_i\}$. The identity lines represent the test benchmark data, and the colored dots represent sequences simulated by different models from simulation level two.

The quantized sequences for the observed sequences and the simulated sequences are compared in terms of the variability measure defined in Sec. 4.4. A smaller variability measure means more closeness of the observed and simulated ones. Tab. 4 shows the mean and variance of the variability measures. The *SIEM/SequentialPCA/MVG* simulations are usually the closest to the original sequences. The *IS-TVF/SequentialPCA/MVG* simulations have considerable variability, which means the simulated sequences include much noise and can become slightly unrealistic. In comparison, the *PWI* simulations have much smaller variability because the simulated sequences are only the mean sequences with some independent random noises. Overall, the *SIEM/SequentialPCA/MVG* simulations replicate the structure of the original data better than the *IS-TVF/SequentialPCA/MVG* and the *PWI* approaches.

Motion Type	Original	Model		
		<i>IS-TVF/SequentialPCA/MVG</i>	<i>SIEM/SequentialPCA/MVG</i>	<i>PWI</i>
Motion 1	0.2911(0.0099)	0.4942(0.0303)	0.3401(0.0045)	0.2110(0.0004)
Motion 2	0.2532(0.0241)	0.4327(0.0452)	0.3085(0.0060)	0.2382(0.0002)
Motion 3	0.2637(0.0201)	0.5592(0.0312)	0.3131(0.0041)	0.1445(0.0003)
Motion 4	0.4949(0.0326)	0.6244(0.0095)	0.5506(0.0093)	0.4005(0.0005)
Motion 5	0.1689(0.0132)	0.3535(0.0372)	0.2260(0.0014)	0.1719(0.0001)

Table 4 Variability of the quantized simulation sequences compared against the original sequences. The table shows mean variability with the variance in the parentheses.

Tab. 5 compares the transition matrices under different estimation settings. The transition matrices are estimated using a sliding window of size of $l = 20$ and step size of $\delta_l = 10$, yielding $29 \times 9 \times 9$ transition matrices. The worst-case scenario of uniform transition matrices ($p_{ij} = 1/9$) is included as a baseline for

comparison. The estimation error for transition matrices is measured by $\|\hat{P} - P^*\|_1$, where \hat{P} is the true and P^* is the generated transition matrix. *IS-TVF/SequentialPCA/MVG* and *SIEM/SequentialPCA/MVG* approaches have smaller differences than the PWI model, with *SIEM/SequentialPCA/MVG* being the smallest.

Motion Type	Model			
	Baseline	<i>IS-TVF/SequentialPCA/MVG</i>	<i>SIEM/SequentialPCA/MVG</i>	PWI
Motion 1	341.500	75.721	65.536	134.790
Motion 2	342.743	104.519	74.306	134.059
Motion 3	347.877	101.480	71.465	144.792
Motion 4	361.628	104.005	105.126	201.111
Motion 5	340.392	118.597	99.359	117.506

Table 5 Difference of the transition matrices. The transition matrices are estimated by a moving interval of 20 and a stepsize of 10. The differences are computed by the L_1 norm, $\|\hat{P} - P^*\|_1$, where \hat{P} and P^* are the estimated matrices from the original sequences and the simulation. The baseline compares the \hat{P} and a worst-case scenario P_0 with uniform distribution, $p_{ij} = 1/9$.

6. Conclusion

We develop a framework to represent sensor-captured human operation motion data and provide a statistical tool to emulate human motion. A bijective mapping is used to flatten motion sequences into multivariate functions. We perform a sequential PCA, including spatial PCA in the linear tangent space and a functional PCA (FPCA) in the temporal space, to transform functions into a set of PCA coefficients. Then, we impose statistical models on these coefficients and emulate new sequences. We conduct several experiments to evaluate different combinations of the flattening and modeling ideas. We measure the quality of simulated motion sequences using several evaluation metrics, including a novel quantization metric. For our datasets, both *integrated single-hop transported vector field* (IS-TVF) and *single inverse exponential map* (SIEM) successfully preserve the main features and simulate realistic motion sequences. In particular, combining SIEM representation, sequential PCA for dimension reduction, and the Gaussian model are best when handling long and complex human motion sequences with limited data.

This framework can provide useful tools: (1) for planning and optimizing human efforts, (2) for a generative model on human shapes in general. Future works include incorporating certain physical restrictions and utilizing weighting factors for different body parts to improve the quality of the simulations further.

Acknowledgments

We acknowledge support for this work from the National Science Foundation (grants # 2132311, 2428742, 2413748) and the Air Force Office of Scientific Research (grant # FA9550-23-1-0673).

References

- Amor BB, Su J, Srivastava A (2015) Action recognition using rate-invariant analysis of skeletal shape trajectories. *IEEE Transactions on Pattern Analysis and Machine Intelligence* 38(1):1–13.
- Barnes RM (1949) *Motion and time study* (Wiley).
- Bataineh M, Marler T, Abdel-Malek K, Arora J (2016) Neural network for dynamic human motion prediction. *Expert Systems with Applications* 48:26–34, ISSN 0957-4174.
- Biloš M, Rasul K, Schneider A, Nevmyvaka Y, Günnemann S (2023) Modeling temporal data as continuous functions with stochastic process diffusion. *International Conference on Machine Learning*, 2452–2470 (PMLR).
- Celledoni E, Eslitzbichler M, Schmeding A (2016) Shape analysis on lie groups with applications in computer animation. *Journal of Geometric Mechanics* 8(3):273–304, ISSN 1941-4889.
- da Silva M, Abe Y, Popović J (2008) Simulation of human motion data using short-horizon model-predictive control. *Computer Graphics Forum* 27.
- Deng X, Sarkar R, Labruyere E, Olivo-Marin JC, Srivastava A (2021) Dynamic shape modeling to analyze modes of migration during cell motility. *arXiv preprint arXiv:2106.05617*.
- Deng X, Sarkar R, Labruyere E, Olivo-Marin JC, Srivastava A (2022) Characterizing cell populations using statistical shape modes. *2022 IEEE 19th International Symposium on Biomedical Imaging (ISBI)*, 1–5.
- Gehrig D, Kuehne H, Woerner A, Schultz T (2009) Hmm-based human motion recognition with optical flow data. *2009 9th IEEE-RAS International Conference on Humanoid Robots*, 425–430 (IEEE).
- Guo C, Zuo X, Wang S, Zou S, Sun Q, Deng A, Gong M, Cheng L (2020) Action2motion: Conditioned generation of 3d human motions. *Proceedings of the 28th ACM International Conference on Multimedia*, 2021–2029, MM '20 (New York, NY, USA: Association for Computing Machinery), ISBN 9781450379885.
- Hamilton JD (1994) *Time Series Analysis* (Princeton University Press).
- Hendrich A, Chow MP, Skierczynski BA, Lu Z (2008) A 36-hospital time and motion study: how do medical-surgical nurses spend their time? *The Permanente Journal* 12(3):25.
- Huang J, Huang DZ, Yang Q, Cheng G (2022) Power iteration for tensor pca. *Journal of Machine Learning Research* 23(128):1–47.
- Jupp PE, Kent JT (1987) Fitting smooth paths to spherical data. *Journal of the Royal Statistical Society. Series C (Applied Statistics)* 36(1):34–46, ISSN 00359254, 14679876.
- Kendall DG (1989) A survey of the statistical theory of shape. *Statistical Science* 4(2):87–99, ISSN 08834237, 21688745.
- Le H (2003) Unrolling shape curves. *Journal of the London Mathematical Society* 68(2):511–526.
- Le Brigant A (2019) A discrete framework to find the optimal matching between manifold-valued curves. *Journal of Mathematical Imaging and Vision* 61(1):40–70.

- Lehrmann AM, Gehler PV, Nowozin S (2014) Efficient nonlinear markov models for human motion. *Proceedings of the IEEE Conference on Computer Vision and Pattern Recognition (CVPR)*.
- Liu J, Ma S, Xu W, Zhu L (2022) A generalized wilcoxon–mann–whitney type test for multivariate data through pairwise distance. *Journal of Multivariate Analysis* 190:104946, ISSN 0047-259X.
- Lu H, Plataniotis KN, Venetsanopoulos AN (2008) Mpca: Multilinear principal component analysis of tensor objects. *IEEE Transactions on Neural Networks* 19(1):18–39.
- Lyu K, Liu Z, Wu S, Chen H, Zhang X, Yin Y (2021) Learning human motion prediction via stochastic differential equations. *Proceedings of the 29th ACM International Conference on Multimedia*, 4976–4984.
- Park C, Do Noh S, Srivastava A (2022) Data science for motion and time analysis with modern motion sensor data. *Operations Research* 70(6):3217–3233.
- Park S, Ryu H, Lee S, Lee S, Lee J (2019) Learning predict-and-simulate policies from unorganized human motion data. *ACM Transactions on Graphics (TOG)* 38(6):1–11.
- Pavlo D, Feichtenhofer C, Auli M, Grangier D (2020) Modeling human motion with quaternion-based neural networks. *International Journal of Computer Vision* 128:855–872.
- Raptis M, Sigal L (2013) Poselet key-framing: A model for human activity recognition. *2013 IEEE Conference on Computer Vision and Pattern Recognition*, 2650–2657.
- Rasul K, Seward C, Schuster I, Vollgraf R (2021) Autoregressive denoising diffusion models for multivariate probabilistic time series forecasting. *International Conference on Machine Learning*, 8857–8868 (PMLR).
- Richard E, Montanari A (2014) A statistical model for tensor pca. Ghahramani Z, Welling M, Cortes C, Lawrence N, Weinberger K, eds., *Advances in Neural Information Processing Systems*, volume 27 (Curran Associates, Inc.).
- Rizzo ML, Székely GJ (2010) DISCO analysis: A nonparametric extension of analysis of variance. *The Annals of Applied Statistics* 4(2):1034 – 1055.
- Sidenbladh H, Black MJ, Sigal L (2002) Implicit probabilistic models of human motion for synthesis and tracking. *Computer Vision — ECCV 2002*, 784–800 (Berlin, Heidelberg: Springer Berlin Heidelberg), ISBN 978-3-540-47969-7.
- Su J, Kurtek S, Klassen E, Srivastava A (2014) Statistical analysis of trajectories on Riemannian manifolds: Bird migration, hurricane tracking and video surveillance. *The Annals of Applied Statistics* 8(1):530 – 552.
- Suhermi N, Prastyo DD, Ali B, et al. (2018) Roll motion prediction using a hybrid deep learning and ARIMA model. *Procedia Computer Science* 144:251–258.
- Urgo M, Tarabini M, Tolio T (2019) A human modelling and monitoring approach to support the execution of manufacturing operations. *CIRP Annals* 68(1):5–8.
- Veeraraghavan A, Srivastava A, Roy-Chowdhury A, Chellappa R (2009) Rate-invariant recognition of humans and their activities. *IEEE Transactions on Image Processing: A Publication of the IEEE Signal Processing Society* 18:1326–39.

- Wang Y, Sheng Y, Wang J, Zhang W (2018) Optimal collision-free robot trajectory generation based on time series prediction of human motion. *IEEE Robotics and Automation Letters* 3(1):226–233.
- Xiang Y, Arora JS, Abdel-Malek K (2012) Hybrid predictive dynamics: a new approach to simulate human motion. *Multibody System Dynamics* 28:199–224.
- Xiang Y, Chung HJ, Kim JH, Bhatt R, Rahmatalla S, Yang J, Marler T, Arora JS, Abdel-Malek K (2010) Predictive dynamics: an optimization-based novel approach for human motion simulation. *Structural and Multidisciplinary Optimization* 41:465–479.
- Xu YT, Li Y, Meger D (2019) Human motion prediction via pattern completion in latent representation space. *2019 16th Conference on Computer and Robot Vision (CRV)*, 57–64 (IEEE).
- Yi S, Krim H, Norris LK (2012) Human activity modeling as brownian motion on shape manifold. *Scale Space and Variational Methods in Computer Vision*, 628–639 (Berlin, Heidelberg: Springer Berlin Heidelberg), ISBN 978-3-642-24785-9.
- Zhang R, Ogden RT, Picard M, Srivastava A (2022) Nonparametric k-Sample test on shape spaces with applications to mitochondrial shape analysis. *Journal of the Royal Statistical Society Series C: Applied Statistics* 71(1):51–69, ISSN 0035-9254.
- Zhang W, Tomizuka M, Bae J (2014) Time series prediction of knee joint movement and its application to a network-based rehabilitation system. *2014 American Control Conference*, 4810–4815.
- Zhang Z, Su J, Klassen E, Le H, Srivastava A (2015) Video-based action recognition using rate-invariant analysis of covariance trajectories. *arXiv preprint arXiv:1503.06699* .

This e-companion provides some details of the simulation. EC.1 presents intermediate steps of the simulation process. EC.2 describes videos of the simulated motion in the supplementary material.

EC.1. Details of the Simulation Process

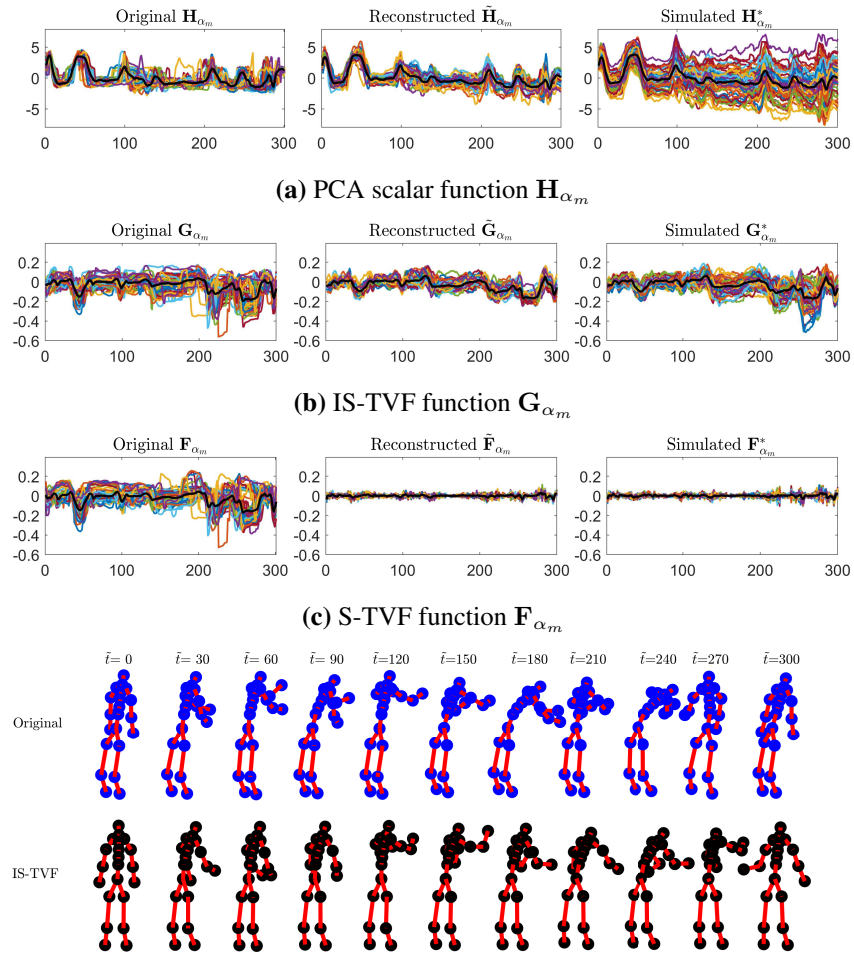
Here, we use the data from motion class one as an example. The simulation uses *IS-TVF/SequentialPCA/MVG* (Fig. EC.1) and *SIEM/SequentialPCA/MVG* (Fig. EC.2) with a set of $d_1 \times d_2 = 10 \times 30$ PCA coefficients. Once a set of PCA coefficients \mathbf{A}^* is generated, one can create a vector-valued function of the spatial PCA coefficients \mathbf{H}^* by $\mathbf{H}^{*(i)} = \boldsymbol{\mu}^{(i)} + \sum_{j=1}^{d_2} a_{ij}^* \boldsymbol{\beta}_j^{(i)}$, where a_{ij}^* is one element of \mathbf{A}^* , $\boldsymbol{\mu}^{(i)}$ and $\boldsymbol{\beta}_j^{(i)}$ are the mean and basis functions of the FPCA as discussed in Sec. 4-2. Subsequently, one can construct the IS-TVF (or SIEM) by $\mathbf{G}^*(t)$ (or $\mathbf{W}^*(t) = \mathbf{m} + \mathbf{U}\mathbf{H}^*(t)$), where \mathbf{m} is the mean vector and \mathbf{U} is the spatial PCA projection matrix as discussed in Sec. 4-2. If IS-TVF is used, one can use finite differences to get S-TVF \mathbf{F}^* and then compute the motion sequence α^* ; if SIEM is used, one can directly map \mathbf{W}^* to the posture space to get α^* (Sec. 4-1). The following figures show some examples of these intermediate functions of the simulation process.

1. *IS-TVF/SequentialPCA/MVG*: Fig. EC.1 shows the detailed simulation process for the *IS-TVF/SequentialPCA/MVG* model. While the simulated spatial PCA coefficient trajectories $\mathbf{H}_{\alpha_m}^*$ (Fig. EC.1a) and IS-TVF functions $\mathbf{G}_{\alpha_m}^*$ (Fig. EC.1b) are similar to the original functions, the simulated S-TVF functions $\mathbf{F}_{\alpha_m}^*$ (Fig. EC.1c) are much smoother than the original functions. Fig. EC.1d shows examples of the simulated sequences α^* . One can see that the simulated sequences are realistic and reasonable compared to the real sequences.

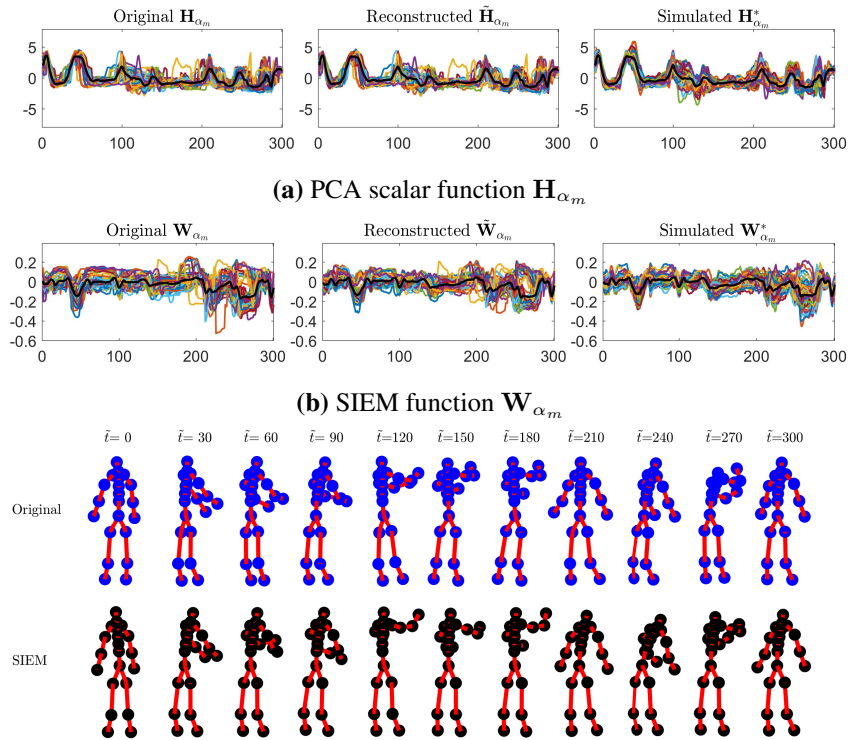
2. *SIEM/SequentialPCA/MVG*: Similar to the previous case, Fig. EC.2 shows the simulation process of *SIEM/SequentialPCA/MVG* model. Fig. EC.2a shows the simulated spatial PCA coefficient trajectories $\mathbf{H}_{\alpha_m}^*$, and Fig. EC.2b shows the SIEM functions $\mathbf{W}_{\alpha_m}^*$. In contrast to the IS-TVF approach, the simulated SIEM functions $\mathbf{W}_{\alpha_m}^*$ have a similar smoothness as the original SIEM functions \mathbf{W}_{α_m} (as shown in Fig. EC.2b) because the SIEM mapping doesn't have extra numerical steps (the differentiating and integrating steps used in IS-TVF reconstructions). Fig. EC.2c shows an example of the simulated sequences α^* . The simulated sequences are also realistic and reasonable compared to the real sequences.

EC.2. Videos of the Simulated Motion

The supplementary material contains videos of the simulated motion. The naming of each video follows the rule of: *[model]_Motion[X]_[Y].mp4*, where *model* is the simulation model including *ISTVF* (stands for *IS-TVF/SequentialPCA/MVG*), *SIEM* (stands for *SIEM/SequentialPCA/MVG*), and *PWI*, *X* is the number of the motion class, and *Y* is the index of the simulated motion. *E.g.*, the file *ISTVF_Motion1_1.mp4* is the first simulated motion of the motion class one generated by the *IS-TVF/SequentialPCA/MVG* model. Each video contains two motions: on the left (black) is the mean motion of the corresponding motion class, and on the right (blue) is the simulated motion. For *IS-TVF/SequentialPCA/MVG* and *SIEM/SequentialPCA/MVG* models, we use a set of 10×30 sequential PCA coefficients.

**Figure EC.1**

Simulated functions and motion sequences of motion class one using *IS-TVF/SequentialPCA/MVG*. From the top to the bottom are one element of the PCA scalar functions \mathbf{H}_{α_m} , one element of the IS-TVF function \mathbf{G}_{α_m} , the same element of the S-TVF function \mathbf{F}_{α_m} , and examples of simulated motion sequences.



(c) An example of the simulated data using the SIEM approach of motion one.

Figure EC.2 Simulated functions and motion sequences of motion class one using *SIEM/SequentialPCA/MVG*. From the top to the bottom are one element of the PCA scalar functions \mathbf{H}_{α_m} , one element of the SIEM function \mathbf{W}_{α_m} , and an example of simulated sequences.